# Zircon U–Pb geochronology, Hf–O isotopes and whole-rock geochemistry of A-type granitoids in Halajun, South Tienshan, NW China: Implications for subdivision, petrogenesis and tectonic settings

Tian-Chu Chen [a,c,d], Ming-Xing Ling [b,*], Yu-Long Liu [d,e,**], Ying Wei [b], Xi-Hui Cheng [b], Xiao-Yan Jiang [f], Shuo Xue [d,e], Ze-Bin Luo [g], Jiang-Hao Bai [a,c,d]

[a] State Key Laboratory of Isotope Geochemistry, Guangzhou Institute of Geochemistry, Chinese Academy of Sciences, Guangzhou 510640, China
[b] State Key Laboratory of Nuclear Resources and Environment, East China University of Technology, Nanchang 330013, China
[c] University of Chinese Academy of Sciences, Beijing 100094, China
[d] CAS Center for Excellence in Deep Earth Science, Guangzhou 510640, China
[e] Key Laboratory of Mineralogy and Metallogeny, Guangzhou Institute of Geochemistry, Chinese Academy of Sciences, Guangzhou 510640, China
[f] State Key Laboratory of Ore Deposit Geochemistry, Institute of Geochemistry, Chinese Academy of Sciences, Guiyang 550081, China
[g] School of Emergency Management, Xihua University, Chengdu 610039, China

## ARTICLE INFO

## ABSTRACT

Abundant A-type granitic intrusions are located within the South Tienshan Orogenic Belt (STOB) and the adjacent area to the Tarim Block. Most of these intrusions share the analogical epoch of the Tarim Large Igneous Province (TLIP), however display diverse alkalinity and geochemical signature. There is controversy in deciphering the subdivision, petrogenesis and geodynamic setting of these intrusions based on their varied geochemical compositions. In this contribution, we conduct integrated research of whole-rock major and trace element compositions, zircon U–Pb geochronology, and in-situ zircon Hf–O isotopic characteristics of several Halajun intrusions in the STOB, to unravel their subdivision, petrogenesis and geodynamics. The Halajun IV quartz-syenite, Kaladuowei quartz-monzonite and tourmaline-rich granite show Permian crystallization ages of $283.4 \pm 1.1$ Ma, $280.2 \pm 1.3$ Ma and $270.7 \pm 1.5$ Ma, respectively. These intrusions exhibit high Zr + Nb + Ce + Y concentrations (449–1592 ppm), $10,000 \times$ Ga/Al values (3.31–4.47), Na$_2$O + K$_2$O (6.9–10.9 wt%), (K$_2$O + Na$_2$O)/CaO (3.5–19.2) and FeO$^T$/(FeO$^T$ + MgO) (0.67–0.95), which are similar to those of typical A-type granitoids. These samples show various degrees of enriched Rb, Th, U, Zr, Hf and Pb, and depleted Ba, Sr and Eu. Decoupling of Nb and Ta in late granitic phases infers that the Nb–Ta differentiation occurred during the magmatic evolution. The in-situ zircon Hf and O isotopes of these intrusions show wide ranges of $\varepsilon_{Hf(t)}$ (−1.2 to +4.7) and $\delta^{18}$O (+6.2‰ to +8.2‰), indicating that crust- and mantle-derived materials were both involved in the quartz-syenite, quartz-monzonite and tourmaline-rich granite. End-member mixing model shows that the mantle contribution is ~80% for quartz-syenite and ~60–65% for quartz-monzonite and tourmaline-rich granite, respectively. With the increasing crustal materials of the parental magma and the subsequent fractionation of ilmenite and biotite, they exhibit a gradual tendency from A$_1$-type to A$_2$-type granitoids. This suggests that A-subtypes may evolve during the magmatic process. Considering the same tectonic setting and a common parental source, the quartz-syenite, quartz-monzonite and tourmaline-rich granite should be A$_1$-type. The Halajun plutons were emplaced between the STOB and Tarim Block, and their generation might be related to the contemporaneous Permian Tarim mantle plume. The primitive magmas, derived from mantle plume, was mixed with the ancient Proterozoic crust and formed the Halajun A$_1$-type granitoids.

These alkaline intrusions share two tectonic regimes, i.e., the southern margin of the Tienshan Orogenic Belt and the northern margin of TLIP. The regional tectonic setting was in the transitional period from a compressive regime to an extensional or post-collisional one in the Late Paleozoic. The rising plume generated the ultramafic pipes, and provided dynamic energy to the extensional motion. The collapse of the Tienshan Orogenic Belt and

---

* Corresponding author.
** Corresponding author at: Key Laboratory of Mineralogy and Metallogeny, Guangzhou Institute of Geochemistry, Chinese Academy of Sciences, Guangzhou 510640, China.
*E-mail addresses:* mxling@ecut.edu.cn (M.-X. Ling), ylliu@gig.ac.cn (Y.-L. Liu).

the contemporary heavy eruption of TLIP not only afforded channels for the upwelling mantle magma, but also cycled the lithosphere or crustal materials into the mantle, which might have been involved in the formation of the A$_2$-type granitoids in the STOB. The A$_1$-type granitoids were mainly derived from the mantle source along the terminal suture.

## 1. Introduction

A-type granitoid is geochemically defined as anhydrous, alkaline, and anorogenic granitoid, which is commonly generated in the extensional tectonic setting, such as continental rifting and post-collisional environments (Bonin, 2007; Collins et al., 1982; Eby, 1990, 1992; Loiselle and Wones, 1979). Further research also suggests that A-type granitoid could be formed under the setting of the particular slab rollback during the subduction process (Collins et al., 2019; Jiang et al., 2020), but these granitoids are not the typical ones occurred along rift zones and within stable continental blocks. A-type granitoids show various compositions from alkaline to metaluminous to peraluminous (Bonin, 2007), generally characterized by high Ga/Al ratios, enrichment of Nb-Ta-Zr-Hf and (Na$_2$O + K$_2$O), and high magmatic temperature. A-type granitoid can be further subdivided into A$_1$- and A$_2$-type granitoid corresponding to different origins and tectonic backgrounds (Eby, 1992). A$_1$-type granitoids have low Y/Nb ratios (<1.2) with geochemical affinities similar to those of oceanic island basalts (OIB) emplaced in the intraplate setting. On the contrary, A$_2$-type granitoids (Y/Nb > 1.2) show chemical characteristics similar to those of continental crust or
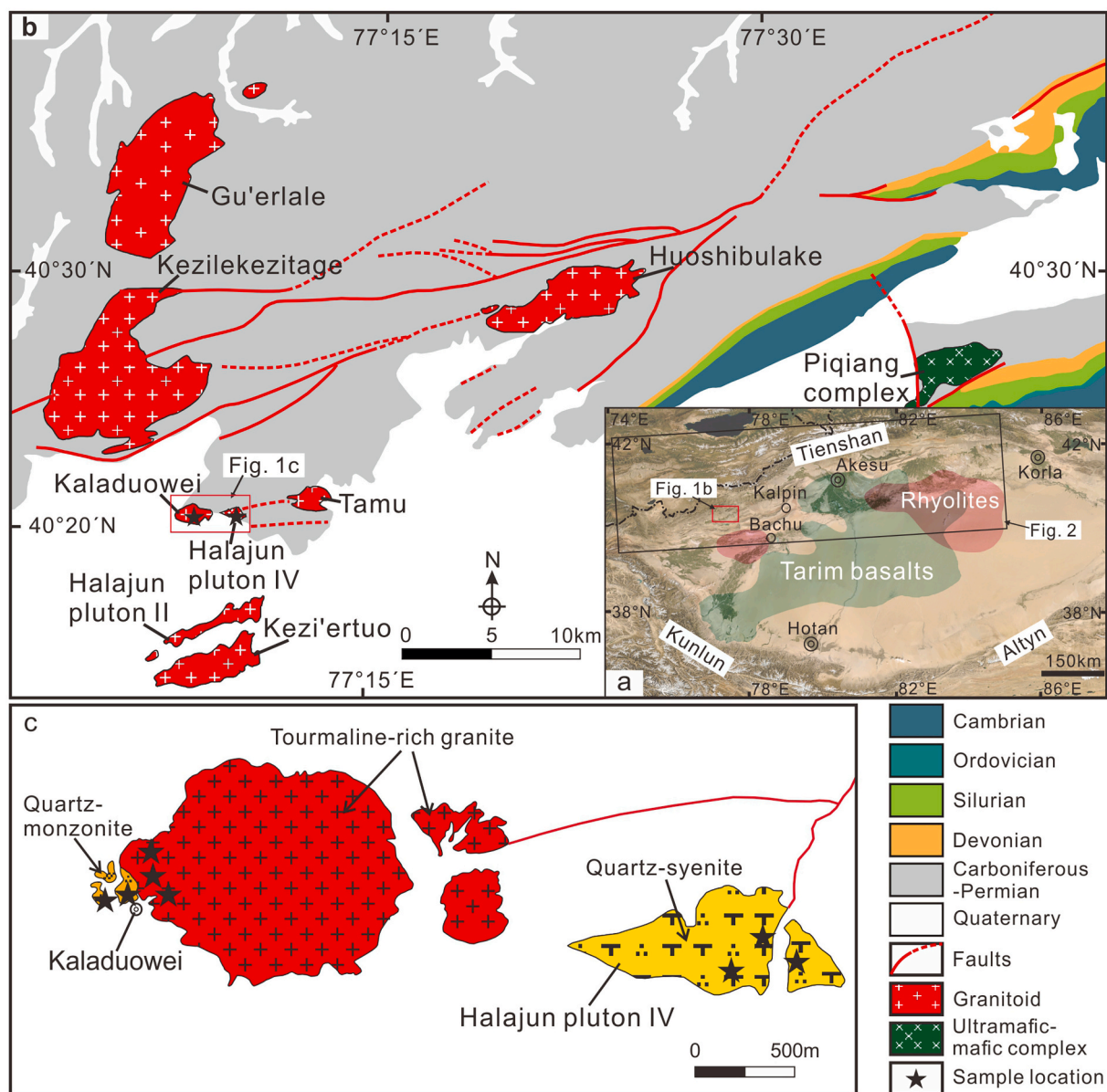


**Fig. 1.** Geographical location of the Halajun plutons within the South Tienshan Orogenic Belt (STOB), NW China. (a) Simplified geological map of Tarim Block, showing the distribution of the Permian basalts, rhyolites and the study area (modified after Yang et al., 2007). (b) Geological map of the Halajun plutons and sample locations. (c) Detailed geological map of the Halajun pluton IV quartz-syenite and Kaladuowei quartz-monzonite and tourmaline-rich granite (based on the field outcrop).
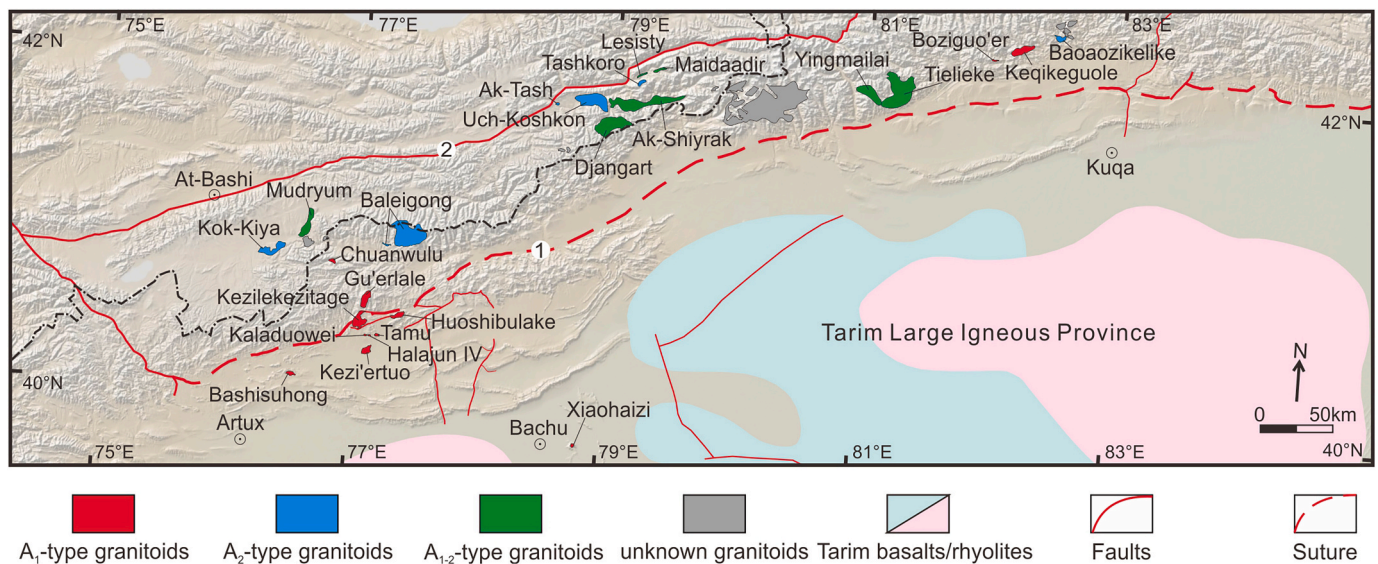
**Fig. 2.** Schematic geological map of the alkaline intrusions belt of STOB. 1- North Tarim Suture; 2- South Central Tienshan Suture.

island arc basalts (IAB) formed at convergent margins. While some A-type granitoids would plot within the field of both $A_1$-type and $A_2$-type granitoids (Frindt et al., 2004; Jiang et al., 2020), transitional A-type ($A_{1-2}$) granitoids and their controlling factors are still obscure. This may be caused by the various crust-mantle interaction, assimilation and contamination (Dobretsov, 2003; Eby, 1992), and fractional crystallization (Eby, 1990).

The Tarim Basin is a stable paleo-continental block in NW China (Fig. 1a), and the A-type granitoids (including $A_1$ and $A_2$ subtype) are widespread around the Tarim Basin and the South Tienshan Orogenic Belt (STOB) from 250 to 300 Ma (Konopelko et al., 2009; Zhang and Zou, 2013), which provide an excellent region to research the A-type granitoid. The $A_1$-type granitoids mainly occurred along the north adjacent area of Tarim Basin, but the $A_2$-type granitoids are emplaced within the STOB (Fig. 2), which attracts debate on their genesis and tectonic settings. Most of the Permian A-type granitoids are proposed to be associated with the post-collisional extension in the STOB (Konopelko et al., 2009; Solomovich and Trifonov, 2002). Whereas some studies revealed higher zircon-saturation temperatures (>800 °C) and geochemical characteristics of intraplate magmatism, suggesting some A-type granitoids have genetic relation with the Tarim mantle plume activity rather than post-collisional extension (Liu et al., 2013; Liu et al., 2014; Liu et al., 2019; Su et al., 2019; Wei et al., 2019; Zhang and Zou, 2013; Zong et al., 2020). Due to the lack of systematic study, the subdivision, genesis, and geotectonic settings of the A-type granitoids are still to be worth researching.

In this study, we present integrated petrology, zircon U–Pb dating, zircon Hf–O isotopic compositions, as well as whole-rock geochemistry to determine the subdivision, petrogenesis, and geodynamic evolution of A-type granitic plutons in the Halajun area (Fig. 1b). In combination with previous studies, we aim to further decipher the mechanism of transformation from $A_1$-type granitoid belt to $A_2$-type granitoid belt in the Tarim Basin and STOB.

## 2. Geological settings

Altay Mountain, Tienshan Mountain and Kunlun Mountain folding the Junggar Basin and Tarim Basin (three mountains folding two basins) is a special terrain in Xinjiang Uyghur Autonomous Region in northwestern China. Statistically, the tectonic and magmatic activities are gradually younger from the northern Central Asian Orogenic Belt (including Altay Mountain and Tienshan Mountain) to the southern Kunlun Mountain (Xiong et al., 2016). The Tienshan Mountain is located

in the middle of the terrain with a transitional magmatic period. The Tienshan Mountain can be divided into the Eastern Tienshan and the Western Tienshan in China, and the Western Tienshan extends westward into the Central Asian countries. The Western Tienshan is further divided into the South Tienshan (Fig. 1a), Central Tienshan and North Tienshan (Allen et al., 1992). Two late Paleozoic suture zones, the North Tienshan suture zone and South Tienshan suture zone (North Tarim Suture and South Central Tienshan Suture, Fig. 2), divide the Chinese part of the Tienshan and adjacent area into the Junggar, the Yili-Central Tienshan and the Tarim plates from north to south (Allen et al., 1992; Gao et al., 1998; Windley et al., 1990).

The South Tienshan is located between the Tarim Block and the Yili Central Tienshan block. The collision between the South Tienshan plate and the Tarim Block constrains the final amalgamation of the Central Asian Orogenic Belt (CAOB), during the Late Paleozoic (Abuduxun et al., 2021). The Silurian-Permian high- and/or ultrahigh-pressure metamorphism belt (Satybaev et al., 2018; Tagiri et al., 1995; Wang et al., 2011b) along the terminal suture (from the Atbashi eclogites and blueschists of Kyrgyzstan in the west to the Heiyingshan-Ouxidaban ophiolitic mélange in the east) is thought to be the products of the subduction of the South Tienshan Ocean and represents a subduction/collision zone between the South Tienshan and the Tarim Block (Klemd et al., 2015). While the timing of the collision has not been reached consensus, the collision is thought to have occurred during the Late Devonian (Charvet et al., 2011), Late Devonian-Early Carboniferous (Wang et al., 2011a), the end of the Early Carboniferous (Zonenshain et al., 1990), the end of the Carboniferous to the Early Permian (Han et al., 2011), and Triassic (Zhang et al., 2007).

The STOB is characterized by thrust-overthrust faults in the west and tight-overturned folds in the east, while the northern and central Tarim Basin is mainly formed by uplifts and depressions. The boundary between the STOB and the Tarim Block is the north Tarim fault (Fig. 2), which is more recognized as the terminal suture (Abuduxun et al., 2021). We name this conjugating occurrence "the Belt and Margin", the South Tienshan Orogenic Belt in the north and the Northern Margin of the Tarim Block in the south. The STOB and the Tarim Block represent two different tectonic settings. The STOB stands for the intensive intracontinental orogeny, which is obviously controlled by the abyssal faults and secondary rifts. Lower Permian molasse sequences develop unconformity over the Carboniferous strata (field observation), which implies the terminal stages of orogenic events, in the north of the Keqikeguole-Baoaozikelike area. Whereas this molasse sequence is not found in other areas. The Tarim Block is one of the largest Precambrian
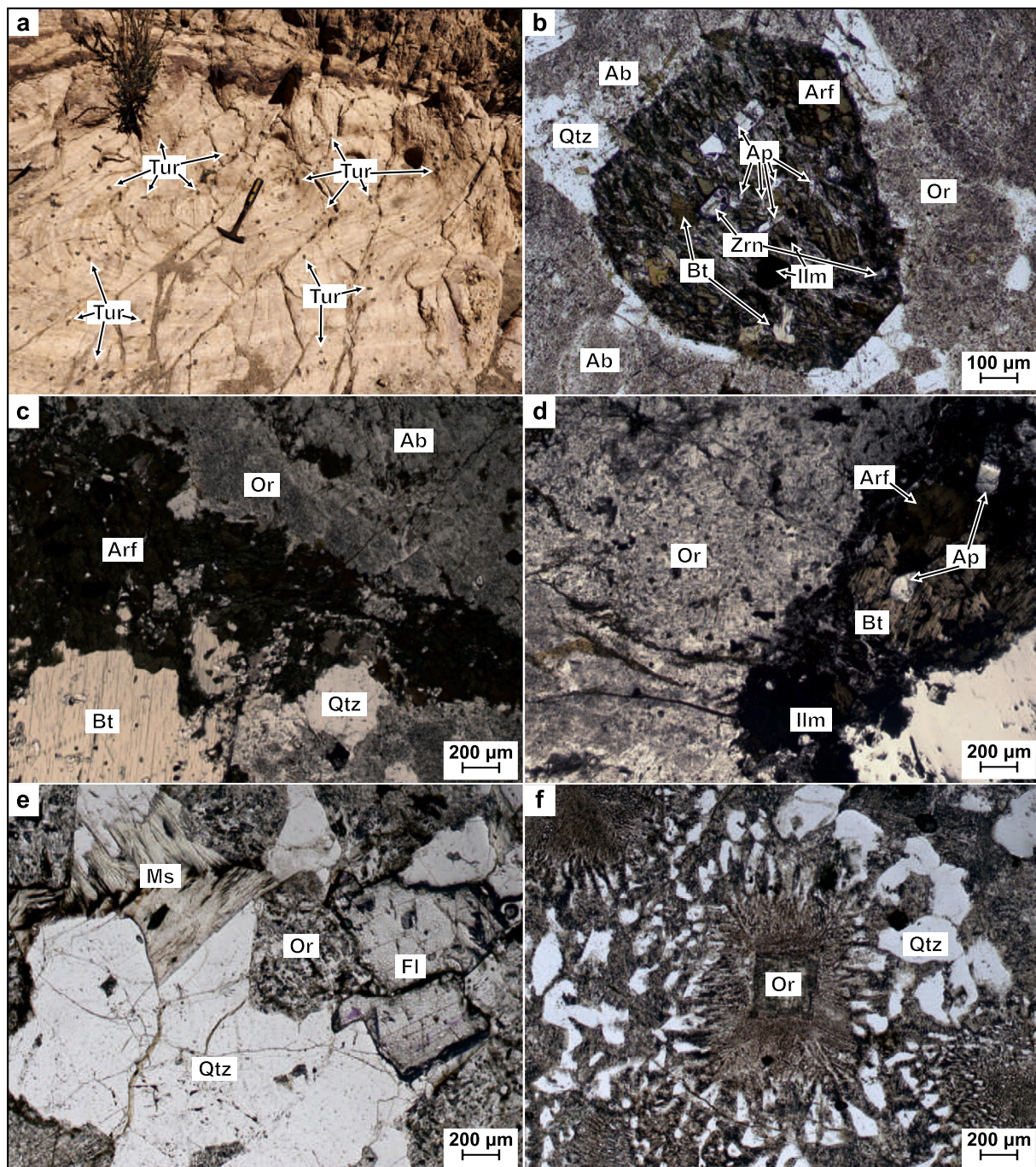
**Fig. 3.** Petrographic and microstructural photographs of the Halajun pluton IV and Kaladuowei granitoids. (a) The outcrop of quartz-tourmaline nodules in the Kaladuowei tourmaline-rich granite; (b) euhedral zircon, apatite and ilmenite, which are the products of early crystallization and intergrowth with arfvedsonite and biotite, in the mafic inclusion of the Halajun pluton IV quartz-syenite; (c) the Halajun pluton IV quartz-syenite containing relatively high amounts of mafic minerals (arfvedsonite, biotite, and ilmenite) and feldspar with an intense kaolinization, and the few anhedral quartzes implies the silicon unsaturated in the magmatic system; (d) microphotographs of the Kaladuowei quartz-monzonite shows euhedral apatite intergrowth with arfvedsonite, biotite and ilmenite; (e) subhedral fluorite crystallizes with feldspar minerals of the Kaladuowei tourmaline-rich granite in the early stage and means the granitic magma rich in fluorite; (f) micrographic textures of the Kaladuowei tourmaline-rich granite indicating the low-T and water-deficient condition of late-stage melt. (Laser Roman and TIMA) Abbreviation: Tur-tourmaline; Ab-Albite; Ap-apatite; Arf-arfvedsonite; Bt-biotite; Ilm-ilmenite; Or-orthoclase; Qtz-quartz; Zrn-zircon; Ms-muscovite; Fl-fluorite.

cratons, where the Early Permian Tarim Large Igneous Province (TLIP) was emplaced, in western China.

The South Tienshan and the Tarim Block record a long span of magmatic history, as follows the major episodes: Neoproterozoic-Cambrian, Ordovician, Late Silurian-Early Devonian, Late Carboniferous-Early Permian and Cenozoic (Seltmann et al., 2011; Yang et al., 2007). Distinctly, the igneous rocks were intensively formed during the Late Carboniferous to Early Permian. Within the period from a compressive regime transformed to an extension or post-collisional regime of the main active stage of the TLIP, the Late Carboniferous-Early Permian is a critical period of magmatic events in the Belt and Margin. The A-type granitoid belt (Fig. 2) was emplaced during the Late Carboniferous to Permian. At the Kok-Shaal Segment (eastern Kyrgyzstan) of Southern Tienshan, the A-type granitoid belt generally

range within a relatively narrow period of 280–300 Ma in the post-collisional settings (Konopelko et al., 2009). These granitoids are associated with coeval tholeiitic mafic rocks and alkaline undersaturated syenites. Some granitic stocks contain locally mafic enclaves with signatures of mingling, like the Tashkoro intrusion, the Mudryum intrusion and the Kok-Kiya intrusion. All these granitic intrusions have similar geochemical attributes. Several of the evolved ones contain Li-mica, polychromatic tourmaline and other rare metal mineral phases, such as the Inylchek complex, the Sukhodol and Komsomol intrusions rich in F, rare metal elements and heavy rare earth elements (Konopelko et al., 2009; Solomovich and Trifonov, 2002). In the Tarim Block, the ~290 Ma flood basalts are widespread across the TLIP, whereas the ultramafic-mafic-felsic intrusions and dyke swarms only occur in the Bachu Uplift and around the margins of the Tarim Block (Li et al., 2011; Wei et al., 2014; Xu et al., 2014; Yu et al., 2011). A-type granitoids were emplaced at the Bachu, Bashisuhong, Halajun and Baicheng counties during the 275–290 Ma (Huang et al., 2012a; Huang et al., 2014; Liu et al., 2014; Liu et al., 2019; Ma et al., 2016; Yang et al., 2007; Zhang and Zou, 2013).

## 3. Sampling and analytical methods

### 3.1. Petrography of the Halajun granitic intrusions

The Halajun region is situated ca. 100 to 130 km northeast of Artux city between Southern Central Tienshan Suture and Northern Tarim Suture. Stratigraphy is well developed, with outcrops from the Cambrian to the Cenozoic strata, and the Kalatieke fracture zones show NE trend in the study area (Fig. 1b). Granitic intrusions (including Huoshibulake, Kezi'ertuo, Halajun pluton II, Tamu, Halajun pluton IV, Kaladuowei, Kezilekezitage and Gu'erlale), outcropping in Halajun region, intruded the Paleozoic strata at 268–278 Ma (Huang et al., 2012a; Su et al., 2019; Wei et al., 2019; Zhang et al., 2010; Zong et al., 2020). In this paper, we choose the Kaladuowei (also named Halajun pluton III) and Halajun pluton IV granitoids, which have less report (Figs. 1c and 3a). Kaladuowei and Halajun pluton IV granitoids roughly emplace in the center of the whole Halajun granitoids intrusions and about 4.5 km west of Tamu intrusion. They are about 500 m apart and approximately east-west trending, covered by Quaternary sediments.

The quartz-syenites of Halajun pluton IV mainly consist of medium- to coarse-grained plagioclase (40–53%), alkali feldspar (25–35%), hornblende + arfvedsonite (8–12%), biotite (8–13%), quartz (6–12%) and minor Fe–Ti oxides (2–4%), fluorite, tourmaline, zircon, and apatite (Fig. 3b–c). Overall, they contain higher contents of Fe–Ti oxides, biotite, amphibole, and plagioclase than the Kaladuowei tourmaline-rich granite.

Based on the field observation, we identify two different gradual lithofacies from the Kaladuowei intrusion and they can be named quartz-monzonite and tourmaline-rich granite from west to east (Fig. 1c). The quartz-monzonite is commonly medium- to coarse-grained. The mineral assemblage consists of plagioclase (35–40%), alkali feldspar (~35%), quartz (18–20%), hornblende + arfvedsonite (~5%), biotite (1–8%), Fe–Ti oxides (1–3%), muscovite (~1%) and accessory mineral including fluorite, tourmaline, zircon, and apatite (Fig. 3d). The tourmaline-rich granites are coarse-grained granitic texture peppered with tourmaline nodules (Fig. 3a), which represents the magmatic origin. Hydrothermal quartz-tourmaline veins are developed in the tourmaline-rich granite. The mineral assemblage consists of plagioclase (25–30%), alkali feldspar (25–35%), quartz (30–40%), muscovite (~3%), Fe–Ti oxides (~1%), biotite (~1%) and accessory mineral including fluorite, tourmaline, zircon, rutile and apatite (Fig. 3e). Micrographic textures are observed (Fig. 3f, intergrowth of K-feldspar and quartz) in the tourmaline-rich granites, indicating the low-T and water-deficient condition of late-stage melt.

### 3.2. Analytical methods

#### 3.2.1. Whole-rock major and trace elements analyses

Each selected fresh sample, 60 g, was powdered to 200 mesh in an agate mortar. The major and trace elements analyses were measured at the ALS Laboratory Group, Analytical chemistry, and testing services. For major elements, the prepared sample was fused with lithium metaborate-lithium tetraborate flux (Lithium Nitrate as the oxidizing agent) and then poured into a platinum mold. The resultant disk was in turn analyzed by X-ray fluorescence (XRF) spectrometry. For trace elements, the samples were divided into two pulp subsamples for analysis. One subsample was digested with perchloric, nitric, and hydrofluoric acids. The residue was leached with dilute hydrochloric acid and diluted to volume. Then, the solution was analyzed by inductively coupled plasma-mass spectrometry (ICP-MS) for ultra-trace level elements. In addition, the same digestion solution was also analyzed by inductively coupled plasma-atomic emission spectrometry (ICP-AES) for trace level elements. Results were corrected for spectral inter-element interferences. The other subsample was added to lithium metaborate/lithium tetraborate flux, mixed well, and fused in a furnace at 1025 °C. The resulting melt was then cooled and dissolved in an acid mixture containing nitric, hydrochloric, and hydrofluoric acids. This solution was then analyzed by ICP-MS. Eight standards (Table S1) were used as external standards for calibrating trace elements abundance. The analytical precision of trace elements is generally better than 8% (relative standard deviation, RSD). According to the actual situation of the sample and the digestion effect, the comprehensive value was the final test result.

#### 3.2.2. Zircon processing procedure

After rock samples were step-by-step smashed to finer to 40–80–120 meshes, zircon grains were separated from representative rock samples using traditional elutriation, magnetic, and density techniques, and then handpicked under a binocular microscope. Single crystal grains were mounted in epoxy resin and polished to expose the internal structures. Transmitted and reflected light micrographs, cathodoluminescence (CL) images, as well as backscattered electron (BSE) images, were used to examine the morphology and internal structure of zircon grains. The BSE and CL imaging were carried out on a field emission scanning electron microscope at Guangzhou Institute of Geochemistry, Chinese Academy of Sciences (GIG-CAS). Three zircon samples of the Kaladuowei and Halajun pluton IV intrusions were selected to do the next analyses.

#### 3.2.3. Zircon O isotopes

Zircon oxygen isotopes were first analyzed using Cameca IMS 1280-HR SIMS at GIG-CAS. $Cs^+$ ion source was used to measure oxygen isotopes by focusing on the analysis spot with a diameter of ~20 μm and nearly a depth of 1–2 μm, $Cs^+$ ion flow ablations negligibly effect on the zircon U–Pb dating and Lu–Hf isotopes. Zircon standard Penglai ($\delta^{18}O_{VSMOW} = 5.31‰$) was used to correct the instrumental mass fractionation factor (Li et al., 2010). The internal precision of a single analysis was generally better than 0.1‰ for $^{18}O/^{16}O$ ratio. The external precision was 3.5% (RSD, Zircon Penglai, $n = 16$, Table S3). Detailed operating conditions and analytical procedures were after the description of Li et al. (2010).

#### 3.2.4. Zircon U–Pb dating

Corresponding to the situ of O isotopic testing points, repolished zircon grains were analyzed by LA-ICP-MS at Wuhan Sample Solution Analytical Technology Co., Ltd. (for quartz-syenite and quartz-monzonite), and by Cameca IMS 1280-HR SIMS at GIG-CAS (for tourmaline-rich granite), respectively. The beam diameter of the LA-ICP-MS is ~32 μm. With regarding to LA-ICP-MS analysis, helium was used as a carrier gas and argon was used as the make-up gas mixing with the carrier gas via a T-conner before entering the ICP. Then, the carrier and make-up gas flows were optimized by ablating NIST SRM 610 to
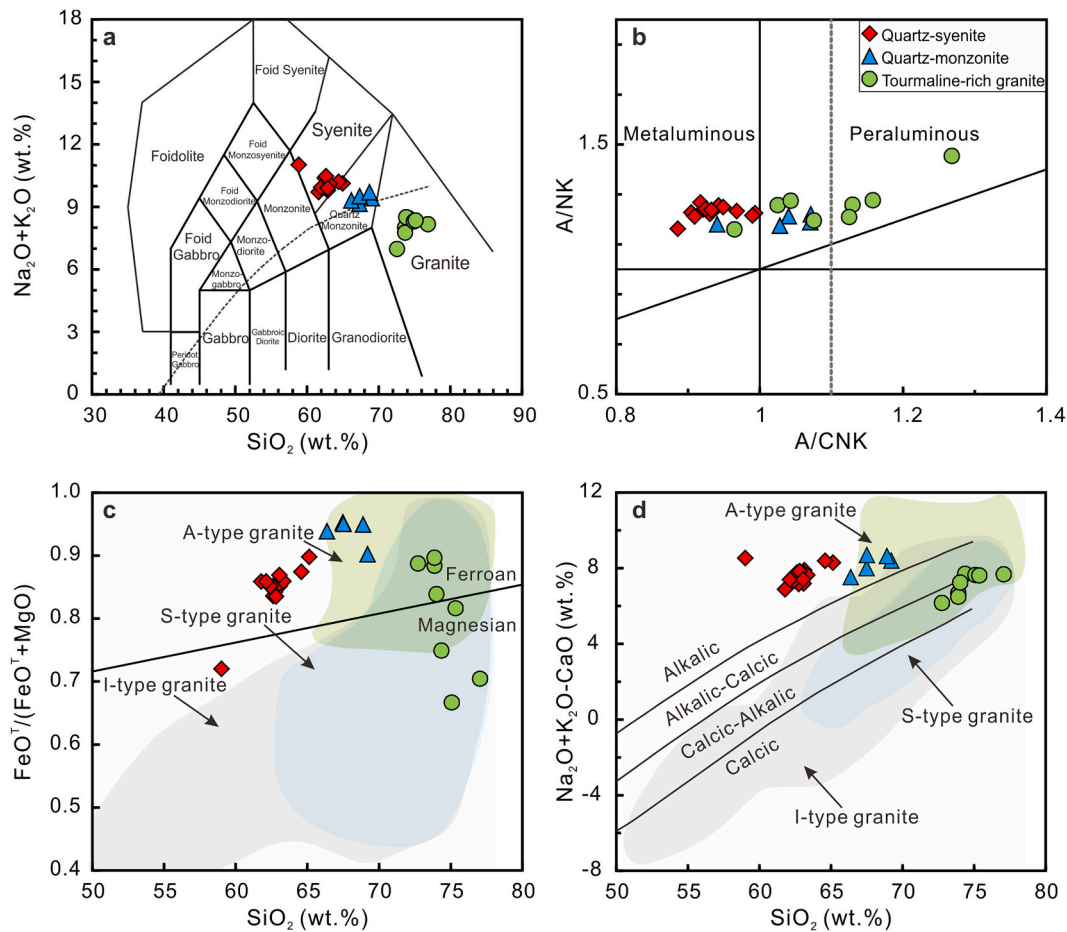
**Fig. 4.** Major-element geochemical classification diagrams for the Halajun pluton IV and Kaladuowei granitoids: (a) Total alkali-silica (TAS) diagram (Lebas et al., 1986; Middlemost, 1994); (b) the alumina saturation (A/NK vs A/CNK) diagram showing the metaluminous to slightly peraluminous from quartz-syenite to quartz-monzonite and to tourmaline-rich granite (Maniar and Piccoli, 1989); (c) whole-rock $FeO^T/(FeO^T + MgO)$ vs $SiO_2$ diagram showing the ferroan nature of the quartz-syenite and quartz-monzonite, and ferroan to magnesian nature of the tourmaline-rich granite (Frost et al., 2001); (d) the MALI ($Na_2O + K_2O$-CaO) diagram (Frost et al., 2001).

optimize the instrument for optimal signal sensitivity and minimum background values. Zircon 91500 was used as an external standard for U–Pb dating. Previous study (Liu et al., 2008; Liu et al., 2010) gave the detailed introduction on the operating conditions and analytical procedures. The analytical procedures of SIMS were after the description of Li et al. (2009). The beam diameter is ~30 μm. The $O_2^-$ primary ion beam was accelerated at 13 kV, with an intensity of ca. 8–10 nA. Positive secondary ions were extracted with a 10 kV potential. In the secondary ion beam optics, a 60 eV energy window was used, together with a mass resolution of ca. 5400 to separate $Pb^+$ peaks from isobaric interference. A single electron multiplier was used in ion-counting mode to measure secondary ion beam intensities by peak jumping. Each measurement consists of 7 cycles. Calibration of Pb/U ratios is relative to the standard zircon Plešovice (337.13 Ma), and the standard zircon Qinghu (159 Ma) provides a suitable reference U–Pb age for the analysis of unknown zircon samples.

### 3.2.5. Zircon Hf isotopes

Lu–Hf isotopic analyses were conducted on the same zircon grains which were previously selected for U-Pb-O measurement by using a Neptune Plus MC-ICP-MS at Wuhan Sample Solution Analytical Technology Co., Ltd. Before the analysis, the samples were polished by ~5 μm to eliminate the influence from previous U–Pb dating. The laser beam diameter was 44 μm with a repetition rate of 5 Hz and an energy density of ~5 J cm$^{-2}$. The detailed description of analytical procedures and calibration methods was published by Hu et al. (2012) and Liu et al.

(2010). Reference zircons 91500 and GJ-1 were used to monitor the accuracy and precision of Hf isotope ratios and instrumental drift with respect to Lu/Hf ratios. The obtained averaged $^{176}Hf/^{177}Hf$ ratios of zircon 91500 and GJ-1 were $0.2823007 \pm 0.0000064$ ($n = 21$, MSWD = 0.35) and $0.2820118 \pm 0.0000064$ ($n = 20$, MSWD = 0.38) respectively, which are consistent with the recommended values (Blichert-Toft, 2008; Morel et al., 2008). The external precision was better than 0.01% (RSD, zircon 91500, n = 21; zircon GJ-1, n = 20). The single stage model ages ($T_{DM1}$) were calculated on the basis of the chondrite model with $^{176}Hf/^{177}Hf = 0.282772$ and $^{176}Lu/^{177}Hf = 0.0332$ (Blichert-Toft and Albarede, 1997) and the depleted mantle model with present-day $^{176}Hf/^{177}Hf = 0.28325$ and $^{176}Lu/^{177}Hf = 0.0384$, respectively (Griffin et al., 2000). The average continental crust with $^{176}Lu/^{177}Hf = 0.015$ (Griffin et al., 2000) was used to calculate two-stage model ages ($T_{DM2}$).

## 4. Results

### 4.1. Whole-rock geochemistry

The whole-rock major and trace element data of these samples are presented in Table S1. The samples consist of 14 Halajun IV quartz-syenite, 5 Kaladuowei quartz-monzonite, and 8 Kaladuowei tourmaline-rich granite.

The Halajun IV and the Kaladuowei granitoids have variable $SiO_2$ (59.01–77.05 wt%), $Na_2O$ (2.51–5.25 wt%), $K_2O$ (3.86–6.96 wt%),
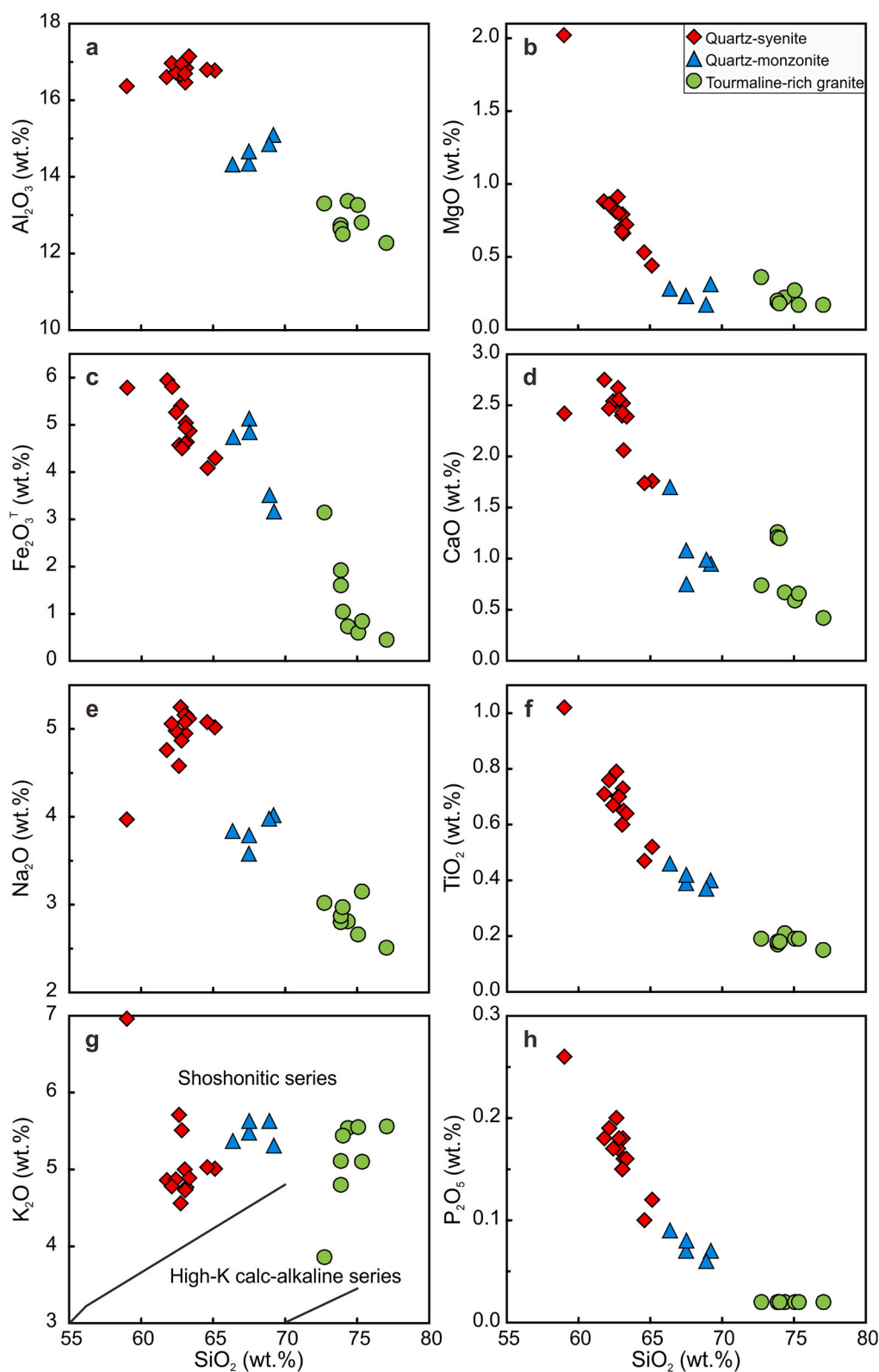
Fig. 5. Covariant diagram of the Halajun pluton IV and Kaladuowei granitoids.

$Fe_2O_3^T$ (0.45–5.94 wt%) and MgO (0.17–2.02 wt%) contents. In the TAS diagram (Fig. 4a), the Halajun IV quartz-syenite samples plot in the syenite field. These samples have relatively high $Al_2O_3$ from 16.36 wt% to 17.14 wt% with A/CNK values from 0.89 to 0.99, plotting in the metaluminous field (Fig. 4b). The Kaladuowei quartz-monzonite and tourmaline-rich granite fall in the quartz-monzonite field and granite field, respectively (Fig. 4a). The Kaladuowei quartz-monzonite and tourmaline-rich granite mainly locate in the peraluminous field (Fig. 4b). Most of these samples belong to the ferroan series in the Fe* ($FeO^T/(FeO^T + MgO)$) diagram (Fig. 4c), except four tourmaline-rich granites. In the MALI ($Na_2O + K_2O-CaO$) diagram (Fig. 4d), quartz-syenite and quartz-monzonite samples fall in the alkalic field, but
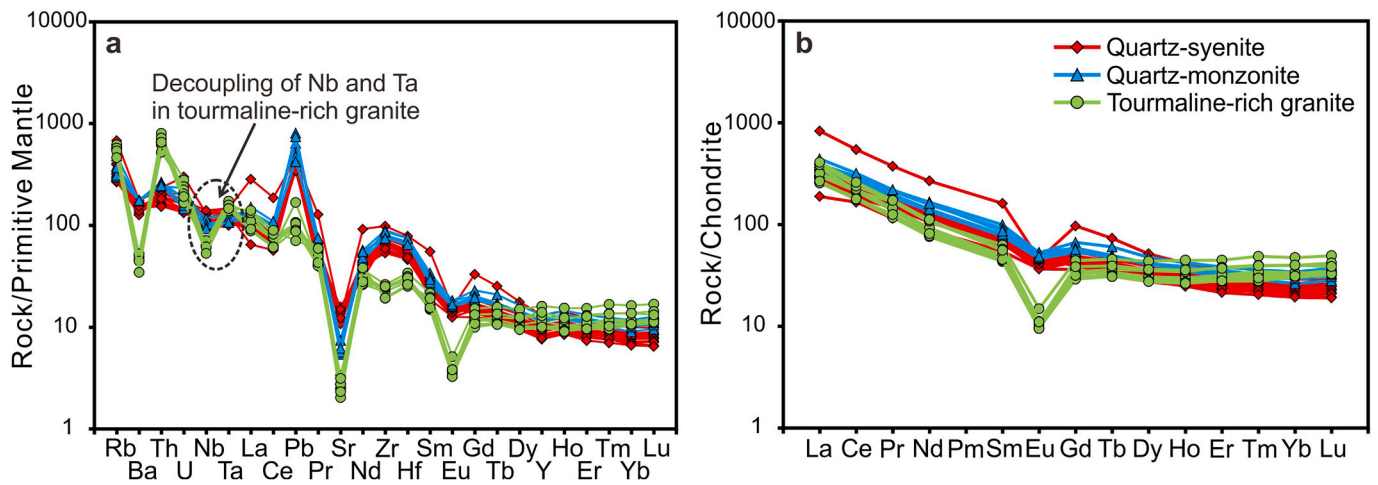
**Fig. 6.** Primitive mantle-normalized trace element spidergrams (a) and Chondrite-normalized REE diagrams (b) of the Halajun pluton IV and Kaladuowei granitoids (Sun and McDonough, 1989).
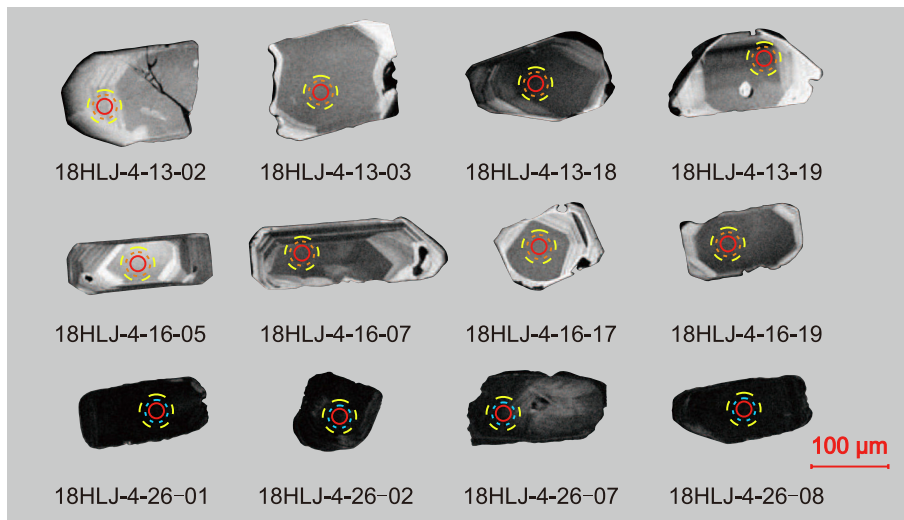


**Fig. 7.** Representative cathodoluminescence (CL) images of zircon grains from the quartz-syenite (18HLJ-4-13), quartz-monzonite (18HLJ-4-16) and tourmaline-rich granite (18HLJ-4-26). Red solid circles indicate SIMS analysis spots for O isotope. Orange and cyan dashed circles indicate the locations of U–Pb dating by LA-ICP-MS and SIMS, respectively. Yellow dashed circles indicate the points of LA-ICP-MS Hf isotopic analyses. (For interpretation of the references to colour in this figure legend, the reader is referred to the web version of this article.)

tourmaline-rich granites mostly aggregate in the calcic-alkalic field.

The contents of $Al_2O_3$, MgO, $Fe_2O_3^T$, CaO, $Na_2O$, $TiO_2$, and $P_2O_5$ of all the samples decrease with the increase of $SiO_2$ content (Fig. 5). This geochemical feature indicates that the quartz-syenite, quartz-monzonite and tourmaline-rich granite underwent similar magmatic evolution originated from a single magmatic series. The contents of $K_2O$ almost remain constant with the increase of $SiO_2$ content from the samples. Except the tourmaline-rich granite plot into both the high-K calc-alkaline and shoshonitic field, the quartz-syenite and quartz-monzonite show the shoshonitic affinities (Fig. 5g).

The Halajun IV and Kaladuowei samples are similarly enriched in high field strength elements (HFSE), and relatively depleted in Ba, Sr, and Eu (Fig. 6a). In the chondrite-normalized REE patterns (Fig. 6b), the quartz-syenite mainly shows various enrichment in LREE with $(La/Yb)_N$ ratios from 9.15 to 28.44, and relatively slight negative Eu anomalies ($\delta$Eu = 0.63–0.89), except one sample ($\delta$Eu = 0.36). The quartz-monzonite has consistent enrichment in LREE ($(La/Yb)_N$ = 10.58–15.33) and negative Eu anomalies ($\delta$Eu = 0.65–0.72). The tourmaline-rich granite exhibits prominent negative Eu anomalies ($\delta$Eu = 0.24–0.28), and has sub-horizontalized HREE patterns ($(La/Yb)_N$ = 6.44–12.80) indicative of absent or limited fractionation of the HREE during the origin or differentiation of its magma. The various Eu anomalies of Halajun IV and Kaladuowei samples could be interpreted as

a result of the presence of plagioclase in the residue or during fractionation.

### 4.2. Zircon U–Pb ages

Zircon U–Pb dating results are presented in Table S2. Most zircon grains are euhedral-subhedral and fall in the range of 100–240 μm length and 100–120 μm width. CL images show that these zircon grains display oscillatory zoning without inherited cores (Fig. 7), indicating a magmatic origin.

Zircon grains from quartz-syenite have variable Th (35–303 ppm) and U (67–327 ppm) concentrations with variable Th/U ratios of 0.5–1.3. Quartz-syenite sample (18HLJ-4-13) gives $^{206}Pb/^{238}U$ ages from 273 to 291 Ma with a weighted mean age of 283.4 ± 1.1 (Fig. 8a–b, N = 15, MSWD = 1.2). Zircon grains from quartz-monzonite show relatively low Th (28–127 ppm) and U (61–178 ppm) concentrations with Th/U ratios of 0.5–0.7. Quartz-monzonite sample (18HLJ-4-16) gives $^{206}Pb/^{238}U$ ages from 270 to 291 Ma and yields a weighted mean age of 280.2 ± 1.3 Ma (Fig. 8c–d, N = 11, MSWD = 2.6). Zircon grains from tourmaline-rich granite display relatively high variable Th (226–907 ppm) and U (526–1315 ppm) concentrations with Th/U ratios of 0.4–0.8. The zircon grains of the tourmaline-rich granite (18HLJ-4-26) give $^{206}Pb/^{238}U$ ages from 261 to 279 Ma and yield a weighted mean
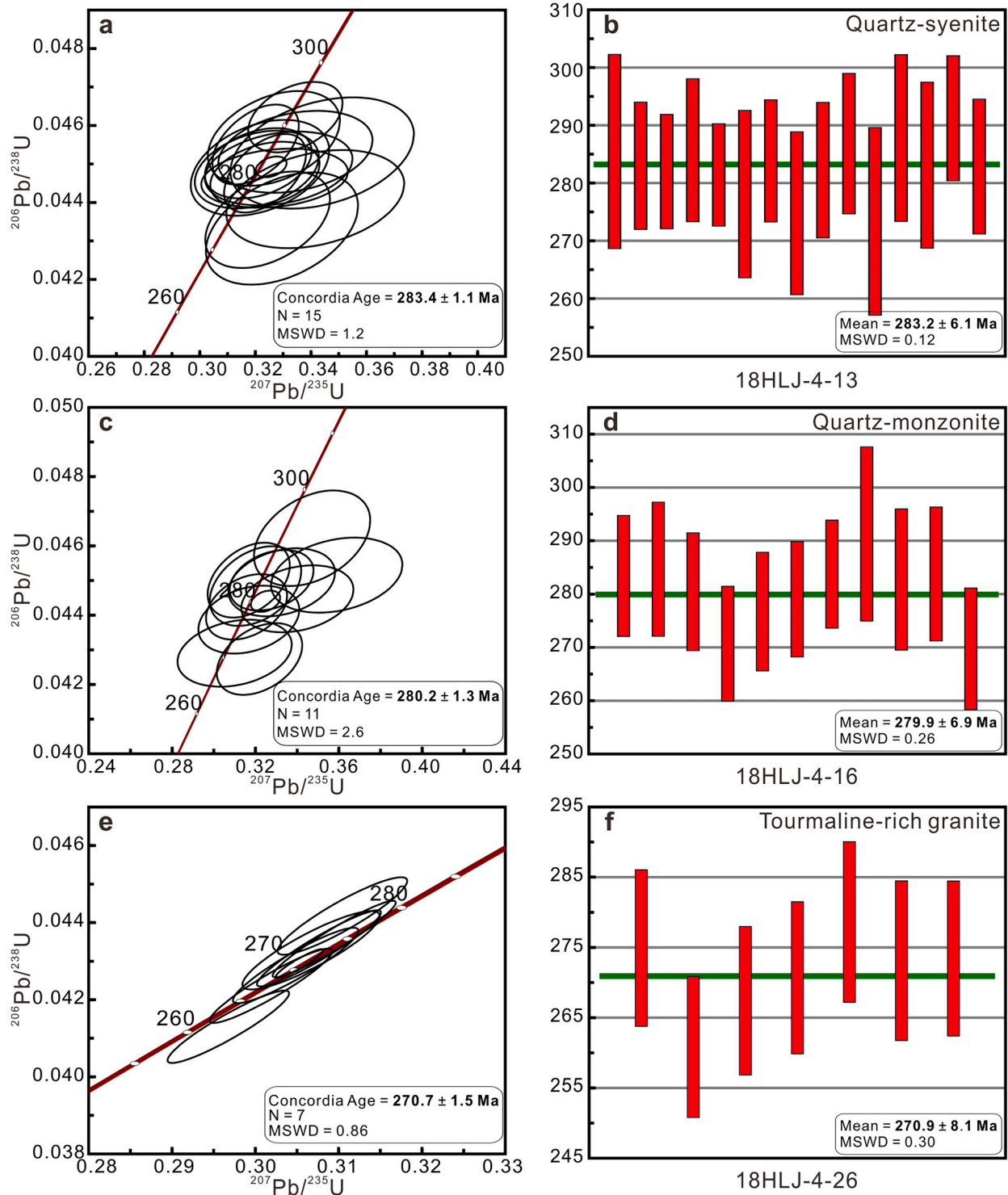
**Fig. 8.** Zircon U–Pb concordia diagrams (a, c and e) and weighted average age results (b, d and f) of the Halajun pluton IV and Kaladuowei granitoids.

age of 270.7 ± 1.5 Ma (Fig. 8e–f, N = 7, MSWD = 0.86). In summary, the results of zircon U–Pb dating indicate that the Kaladuowei and Halajun pluton IV intrusions were formed in the Early Permian.

### 4.3. Zircon Hf and O isotopic compositions

Zircon O-isotope data and Lu–Hf isotope data are presented in Table S3. Zircon grains from these samples show $\delta^{18}O$ values ranging from 6.2‰ to 6.9‰ (quartz-syenite), 7.7‰ to 8.2‰ (quartz-monzonite)

and 7.6‰ to 7.8‰ (tourmaline-rich granite), respectively, higher than the mantle value (5.3 ± 0.3‰) (Valley et al., 1998). Ten zircon grains from the Halajun pluton IV quartz-syenite have a relatively narrow range of initial $^{176}Hf/^{177}Hf$ values of 0.282728–0.282784 and positive $\varepsilon_{Hf(t)}$ values from +4.7 to +6.6 (Fig. 9a), corresponding to the Neoproterozoic crustal model ages ($T_{DM2}$ = 882–1008 Ma). Ten zircon grains of Kaladuowei quartz-monzonite have initial $^{176}Hf/^{177}Hf$ values of 0.282561 to 0.282699 with positive $\varepsilon_{Hf(t)}$ values +0.5 to +3.6, except one point is −1.2 (Fig. 9b), and Mesoproterozoic crust model ages
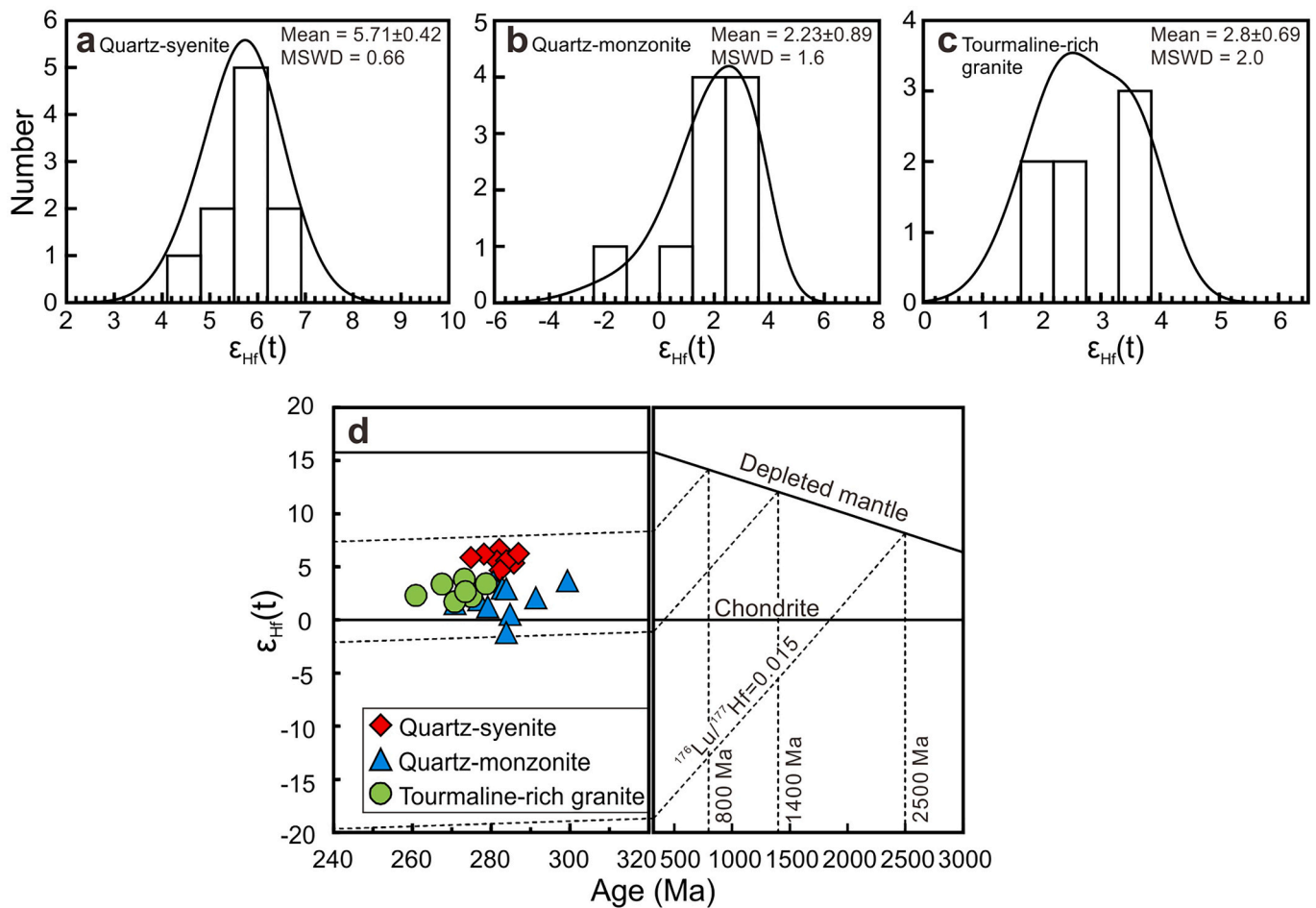
**Fig. 9.** Histograms and relative probabilities of zircon $\varepsilon_{Hf(t)}$ values of the quartz-syenite (a), quartz-monzonite (b) and tourmaline-rich granite (c), respectively. Relationship between zircon $\varepsilon_{Hf(t)}$ values and zircon U–Pb ages of the Halajun pluton IV and Kaladuowei granitoids (d).

($T_{DM2}$) between 1074 and 1383 Ma. Seven zircon grains from Kaladuowei tourmaline-rich granite yield initial $^{176}Hf/^{177}Hf$ values of 0.282651–0.28271 and positive $\varepsilon_{Hf(t)}$ values +1.7 to +3.8 (Fig. 9c), which correspond to Mesoproterozoic crust model ages ($T_{DM2}$ = 1054–1187 Ma).

## 5. Discussions

### 5.1. Petrogenesis of the Halajun granitoids

These granitoids exhibit high values of $Na_2O + K_2O$ (6.9–10.9 wt%), $(K_2O + Na_2O)/CaO$ (3.5–19.2) and $FeO^T/(FeO^T + MgO)$ (0.67–0.95). They display high Zr + Nb + Ce + Y contents (449–1592 ppm), and $10,000 \times$ Ga/Al values (3.31–4.47), consistent with typical features of A-type granitoid (Fig. 10a–b). Based on the zirconium saturation thermometry (Boehnke et al., 2013), the calculated $T_{Zr}$ values of these samples range from 790 °C to 960 °C (Table S1), which is also consistent with the high magmatic temperature of the A-type granitoid. In the three-fold subdivision of Eby (1992), these intrusions mainly belong to the $A_1$-type (Fig. 10c–d). But from the quartz-syenite to quartz-monzonite and to tourmaline-rich granite, it also shows a tendency towards $A_2$-type.

Several mechanisms have been suggested to explain the origin of the Halajun A-type granitoids, e.g., fractionation of mantle-derived magma (Zhang et al., 2010), melting of deep continental crust (Huang et al., 2012a; Su et al., 2019; Zong et al., 2020), and mixing between crustal- and mantle-derived melts (Wei et al., 2019). These synchronous Halajun granitoids have similar Nd isotopic signature (Huoshibulake −2.9 to

−1.8, Kezi'ertuo −0.4 to −0.2, Halajun pluton II -1 to 0, Tamu −2.6 to 0.7, Kezilekezitage −2.6 to −0.4 and Gu'erlale −2.1 to 1.9) and geochemical features (Huang et al., 2012a; Wei et al., 2019; Zhang and Zou, 2013), which support the fractionation model from the primitive mafic magma, like the Piqiang ultramafic-mafic complex (Huang et al., 2012a; Zhang and Zou, 2013). However, this model cannot explain such a large range of zircon $\delta^{18}O$ values (6.2‰–8.2‰) and $\varepsilon_{Hf(t)}$ (−1.2 − +6.6). The Hf–O isotope of Halajun plutons is different from the Piqiang ultramafic-mafic complex (Fig. 11; Zhang et al., 2016). The $\varepsilon_{Hf(t)}$ of the Halajun pluton IV and Kaladuowei granitoids are mainly positive values (Fig. 9), but the values of the Piqiang ultramafic-mafic complex are most negative (average −1.21), indicating a relatively enriched end-member. The positive Hf isotope values also suggested the dominant source are not only Paleoproterozoic basement and meta-sediments. The $\delta^{18}O$ values (6.2–6.9‰) of the quartz-syenite are marginally higher than the mantle value (5.3 ± 0.3‰), which suggest the more contribution of the mantle melt for the formation of the quartz-syenite. The OIB-like chemical signature (Fig. 10c) and ancient two stage Hf model ages of these Halajun intrusions imply the interaction of Tarim plume with ancient materials from lower crust or subcontinental lithospheric mantle in the sources.

Here we choose the average depleted mantle with $\delta^{18}O$ value of 5.3‰ and $\varepsilon_{Hf(t)}$ value of +10.2 and the Kuruktag Late Paleoproterozoic meta-sedimentary rocks ($\varepsilon_{Hf(t)}$ = −9, $\delta^{18}O$ = 12‰) as crustal end-member (Ge et al., 2015). Two end-member modeling suggested that the mantle contribution was ~80% for quartz-syenite and 60–65% for quartz-monzonite and tourmaline-rich granite (Fig. 11). In the Bashisuhong, synchronous igneous carbonatite contains plentiful xenolith
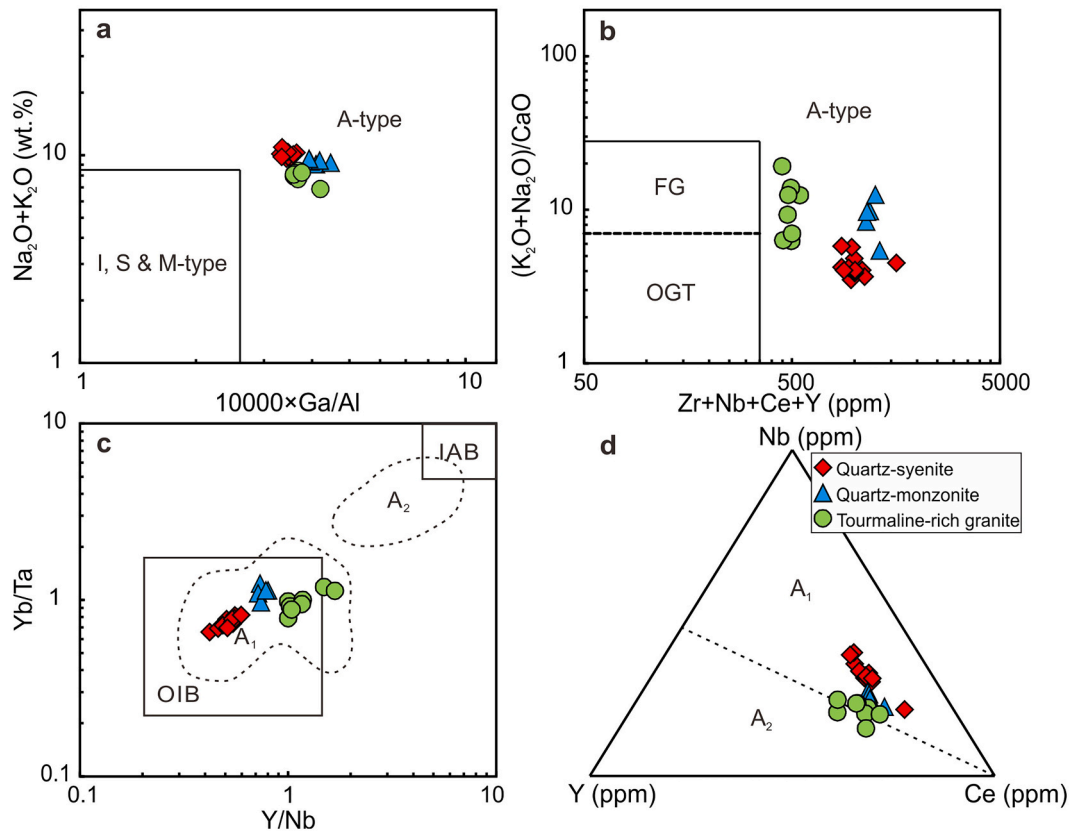
**Fig. 10.** Geochemical classification diagrams for the Halajun pluton IV and Kaladuowei granitoids: (a) Na₂O + K₂O vs 10,000 × Ga/Al and (b) (Na₂O + K₂O)/CaO vs Zr + Nb + Ce + Y (Whalen et al., 1987); (c) Yb/Ta vs Y/Nb and (d) Nb-Y-Ce diagram (Eby, 1992). Abbreviation: FG-fractionated felsic granites; OGT-unfractionated M-, I- and S-type granites; IAB-island arc basalts; OIB-ocean island basalts.
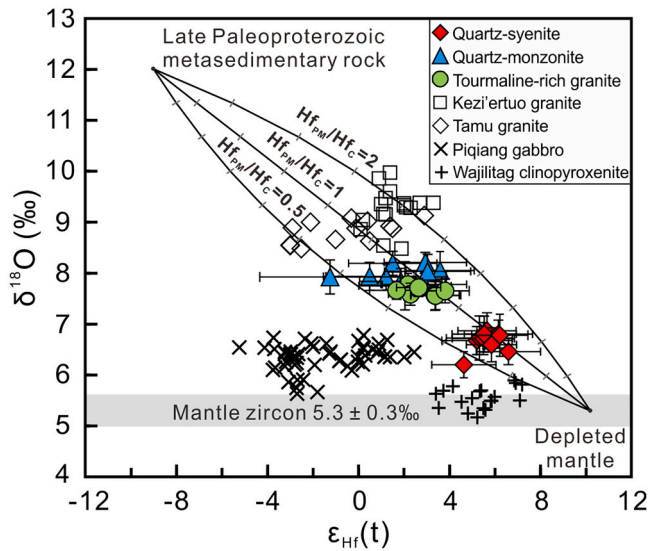


**Fig. 11.** End-member mixing model: $\delta^{18}O$ vs $\varepsilon_{Hf(t)}$ for zircons of the Halajun pluton IV and Kaladuowei granitoids. Error bars are 2σ for $\delta^{18}O$ and $\varepsilon_{Hf(t)}$. The lines denote two-component mixing trends between the mantle- and crust-derived magmas. The $\delta^{18}O$ and $\varepsilon_{Hf(t)}$ values of the mantle-derived melt are 5.3‰ and 10.2, respectively. The $\delta^{18}O$ and $\varepsilon_{Hf(t)}$ values of crustal end-member from the Late Paleoproterozoic metasedimentary rocks are 12‰ and −9, respectively (Ge et al., 2015). Zircon Hf–O data of Kezi'ertuo granite and Tamu granite are from Wei et al. (2019). Zircon Hf–O data of Piqiang gabbro and Wajilitag clinopyroxenite are from Zhang et al. (2016).

zircons. The zircon U–Pb ages ranging from 1337 to 2521 Ma (unpublished data) support that a Proterozoic basement exists at the Bashisuhong-Halajun-Piqiang region, and provides the crustal materials during the Permian magmatism.

Whereas the higher Rb/Sr and lower Nb/Ta and Eu/Eu* ratios (average of 6.57, 7.3 and 0.26, respectively) of the tourmaline-rich granites, relative to lower Rb/Sr and higher Nb/Ta and Eu/Eu* ratios of the quartz-syenite (Rb/Sr = 0.75, Nb/Ta = 15.7, Eu/Eu* = 0.73) and quartz-monzonite (Rb/Sr = 1.8, Nb/Ta = 15.4, Eu/Eu* = 0.7) portray that these tourmaline-rich granites could be distinguishable in sources and fractionating processes (Fig. 12). The highly differentiated chemistry of the tourmaline-rich granites makes them more susceptible to crustal contamination due to their prolonged crystallization (Fig. 12c). The tourmaline-rich granites and quartz-monzonites show similar zircon Hf–O isotopes (Figs. 9 and 11), and their whole-rock trace element ratios are more like the Tarim basement (Fig. 12c). But the tourmaline-rich granites show more middle- to upper-crustal contamination during the prolonged magmatism, and quartz-syenites are mainly affected by lower crust. In the Th/La versus Nb/La diagram (Fig. 12c), the quartz-syenite, quartz-monzonite and tourmaline-rich granite straddle between the field of TLIP mafic-ultramafic rocks and Tarim basement, which further supports the crust-mantle interaction model.

The covariant diagram of these samples shows a single evolutionary trend (Fig. 5), which indicates different degrees of fractional crystallization. The CaO and MgO contents decrease with the increasing SiO₂ (Fig. 5b and d) in response to the crystallization of high-pressure minerals such as calcic-rich amphibole and calcic-rich pyroxene (Hole, 2018). The quartz-syenites, quartz-monzonites and tourmaline-rich granites show evolution trends linearly along plagioclase, K-feldspar and plagioclase + biotite eutectics in the large ion lithophile elements (LILE) bivariate plots (not shown). Significant feldspar fractionation
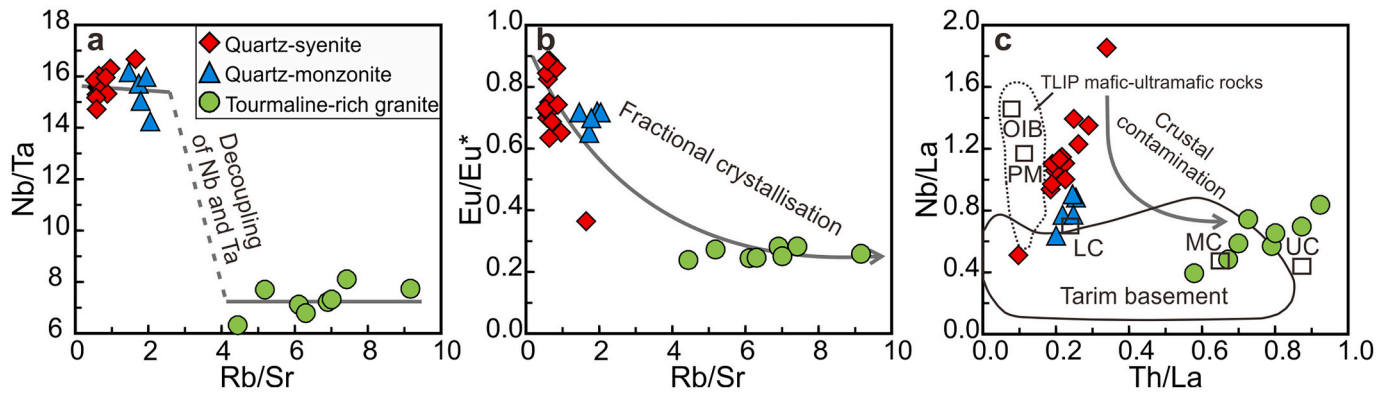
**Fig. 12.** Covariant ratios of trace elements for the quartz-syenite, quartz-monzonite and tourmaline-rich granite. Data of the Tarim basement, TLIP mafic-ultramafic rocks, oceanic island basalt (OIB), primitive mantle (PM), lower crust (LC), middle crust (MC) and upper crust (UC) are from Liu et al. (2014, 2019 and references therein).

consequently depletes the magma in Eu and further consumes CaO. Similarly, the crystallization of feldspars drives the tourmaline-rich granites along an approximate parallel trend to the calcic-alkali boundary (Fig. 4d). Fractionation of titanium-bearing accessory minerals such as ilmenite and apatite accounts for the marked negative Ti and P anomalies, and the decreasing contents of $P_2O_5$ and $TiO_2$ (Fig. 5f and h). The negative correlation between the $Fe_2O_3^T$ and $SiO_2$ content also identifies with that the less evolved quartz-syenite and quartz-monzonite have relatively high Fe–Ti oxide than the tourmaline-rich granite (Fig. 5c). From the less evolved quartz-syenite and quartz-monzonite to the evolved tourmaline-rich granite, there are decoupled of the Nb and Ta systems in the late stage of the granitic phase (Figs. 6a and 12a). The content of Ta is enriched in tourmaline-rich granitic phase with the precipitation of the Fe–Ti oxide in the quartz-monzonitic phase, which is supported by the negative correlations between Ta versus $Fe_2O_3^T$ and $TiO_2$ (Fig. 13a–b).

### 5.2. Transition from A₁- to A₂-subtype granitoid: contributions of source heterogeneity and fractional crystallization

In within-plate settings of intracontinental rift zones, the formation of A₁-type granitoid is generally related to mantle melts or plumes and A₂-type granitoid is resulted from the interaction of mantle melts with felsic continental crustal materials (Dobretsov, 2003). Thus, the differences in the compositions of A₁- and A₂-type granitoids depend on the various proportion of crustal materials involved in the magma during the mantle melts arriving at the upper lithospheric levels. Furthermore, the stability of fractionating mineral phases and prevailing physical and chemical conditions of the magma could also make compositional gaps (Chappell, 1996; Markl et al., 2010). The Halajun transitional A-type (A₁₋₂) granitoids may reflect a particular diagenetic process.

During the Permian, the synchronous A₁-type and A₂-type granitoids (270–300 Ma) are widespread outcrop at the South Tienshan (Fig. 2). A₁-type intrusions are mostly distributed along the terminal suture and close to the TLIP, like the Bashisuhong, Halajun plutons, Chuanwulu, Xiaohaizi, Boziguo'er and Keqikeguole granitoids (Huang et al., 2012b; Huang et al., 2014; Long et al., 2008; Ma et al., 2016; Su et al., 2019; Yang et al., 2007; Zhang et al., 2010; Zong et al., 2020). The A₂-type granitoids, such as the Kok-Kiya, Baleigong, Uch-Koshkon, Ak-Tash, Tashkoro, Xiaotikanlike and Baoaozikelike granite, are located at the northern part of the terminal suture and far from the center of the TLIP (Huo et al., 2019; Konopelko et al., 2007; Konopelko et al., 2009; Long et al., 2008). And a large quantity of the transitional A-type (A₁₋₂) granitoids are crudely distributed between the A₁-type and the A₂-type granitoids, e.g., Mudryum, Djangart, Ak-Shiyrak, Lesisty, Maidaadir, Yingmailai and Tielieke granites (Fig. 2). The whole-rock $\varepsilon_{Nd(t)}$ (Fig. 14) and zircon $\varepsilon_{Hf(t)}$ values of these A-type granitoids show an overall

downward trend from inner TLIP towards STOB (Konopelko et al., 2007; Zhang and Zou, 2013). Such spatial distribution of A-type granitoids may indicate that the mixing proportion between mantle magmas and crust materials controls the transition from the A₁-type granitoid belt to the A₂-type granitoid belt in the STOB.

The Y/Nb ratio is used as the discriminant factor, because the relatively constant character of Y/Nb is mainly controlled by the source (Eby, 1990, 1992). The relatively high Y/Nb ratio (≥2) of the continental crust and the gradual tendency from metaluminous to peraluminous of the Halajun pluton IV quartz-syenite to the Kaladuowei quartz-monzonite and tourmaline-rich granite (Fig. 4b) also agree with more crustal components involved in the source. Whereas the Kezi'ertuo and Tamu granites have higher zircon $\delta^{18}O$ values (8.5–10.0‰, Fig. 11), and their samples mainly have the metaluminous A₁-type granite affinity (Wei et al., 2019). There seems not to agree with the tendency towards A₂-type and the peraluminous character is caused only by the interaction with more crustal components. An alternative mechanism is required to explain the increase in Y/Nb.

As high ilmenite/biotite-melt partition coefficients of Nb (45.3–73.6 and 1.9–9.2) (Acosta-Vigil et al., 2010; Fedele et al., 2015; Nash and Crecraft, 1985; Stepanov and Hermann, 2013; Xiong et al., 2011), the influence of crystallization differentiation of ilmenite and biotite on the Nb/Ta decrease is significant (Ballouard et al., 2020). The fractional crystallization of these minerals could significantly decrease the concentration of Nb in the late magma. The $Fe_2O_3^T$ and $TiO_2$ show a negative correlation with the $SiO_2$ (Fig. 5c and f), implying the fractional crystallization of the ilmenite. The decrease of the ilmenite and biotite from the Kaladuowei quartz-monzonite to tourmaline-rich granite can be observed under the microscope (Fig. 3d–f). In the late granitic phases, there are also decoupled Nb–Ta systems (Figs. 6a and 12a). As the fractional crystallization of the ilmenite and biotite, the Nb/Ta ratios of the Halajun pluton IV and the Kaladuowei also show the decreased trend (Fig. 13c–d), but the samples have a narrow concentration of Y. This would increase the Y/Nb ratios in the late Kaladuowei tourmaline-rich granite (Fig. 13e–f), and result in the geochemical drift and an A₂-type tendency. The biotite K-feldspar granite of the Yingmailai transitional A-type granites also shows more ilmenite than the two-mica K-feldspar granite (Ma et al., 2009). Thus, the various crust-mantle interaction and fractional crystallization could be the main reasons making the geochemical change of the Halajun pluton IV and Kaladuowei granitoids. The transitional A-type granitoids might be cause by the drift of geochemical plot, and their classification should be considered consistent with their tectonic attributes and parental sources. We therefore prefer that the Kaladuowei tourmaline-rich granites belong to the A₁-type granite.

Given the felsic rocks correspond to a wide spectrum of compositions, they classified under the 'A-type' is ambiguous. We suggest that
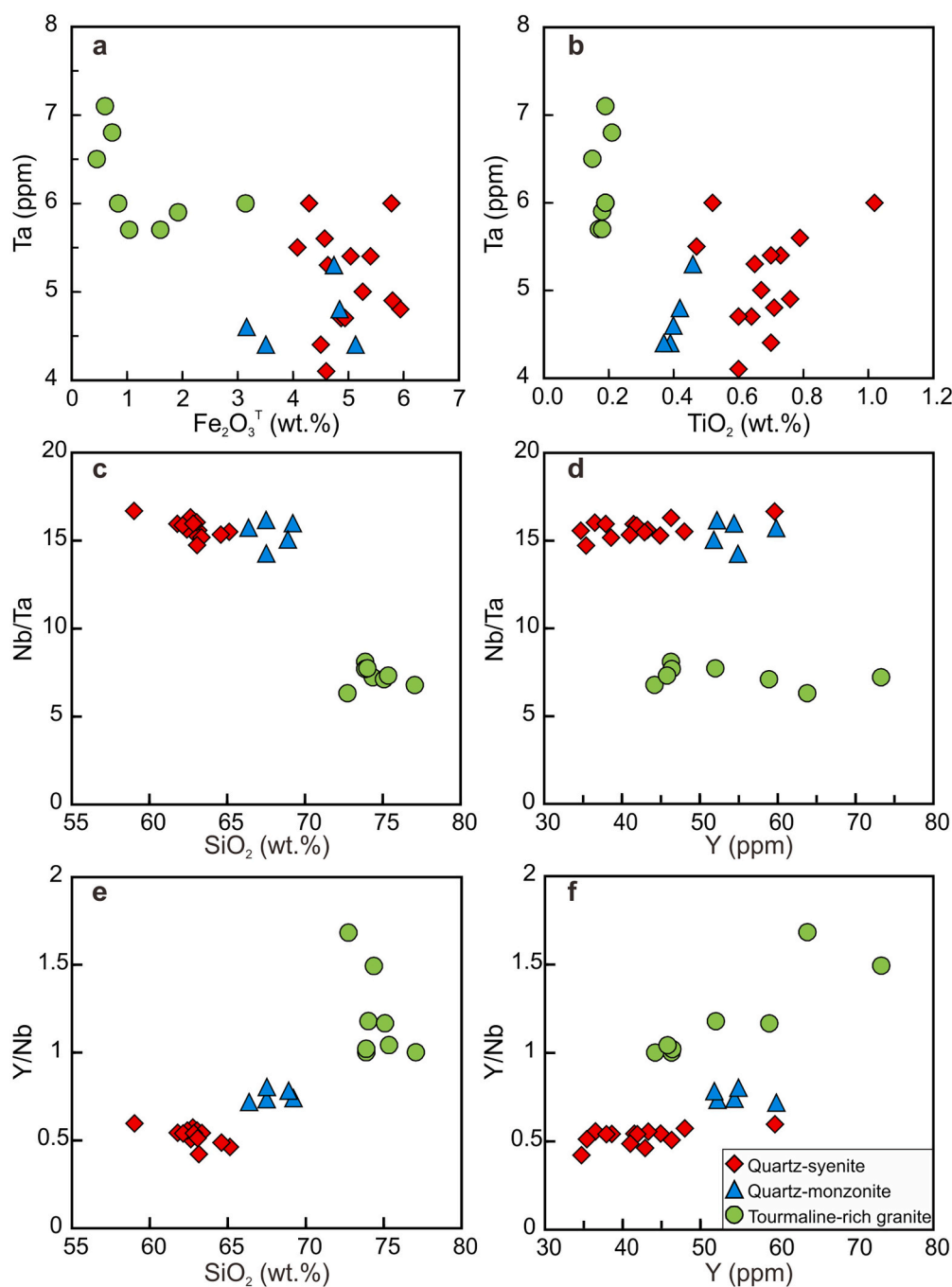
**Fig. 13.** Evolution trend of niobium, tantalum and yttrium in magmatic processes. Ta vs (a) $Fe_2O_3^T$ and (b) $TiO_2$; Nb/Ta vs (c) $SiO_2$ and (d) Y; Y/Nb vs (e) $SiO_2$ and (f) Y.

tectonic attributes are as important as the chemical subdivision to discriminate A-type granitoid and its subtypes, and in-situ zircon Hf and O isotopic characteristics could provide more parental magmatic evidence for the classification of A-type granitoids.

### 5.3. Geodynamic model for the generation of the Halajun granitoids

The nature of the Early Permian tectonic evolution along the northern Tarim Block has long been debated. For the Paleozoic volcanic-sedimentary strata of the South Tienshan, they were interpreted as part of the Tarim passive continental margin (Gao et al., 1998; Han et al., 2011) or a wide accretionary complex formed by the subduction of Paleo-Tienshan (Jiang et al., 2014; Xiao et al., 2015). Different

interpretations of the tectonic nature of the plate margin obscure the evolution of the STOB. Two major geodynamic models of the A-type granitoids including: (1) mantle plume or intracontinental rift (Huang et al., 2012a; Liu et al., 2013; Liu et al., 2014; Liu et al., 2019; Su et al., 2019; Wei et al., 2019; Zhang and Zou, 2013; Zong et al., 2020). (2) post-collisional environment (Han et al., 2011; Konopelko et al., 2009; Long et al., 2011).

The granitoids are mainly emplaced in the within plate tectonic setting and the occurrence of the $A_1$-type granitoids in the Halajun region supports the mantle plume model: (1) In the Permian, the magmatic activities were extremely extensive in the Tarim mantle plume (~300 to ~280 Ma) (Xu et al., 2014). According to the Permian Tarim mantle plume model, two prominent magmatic episodes were emplaced at
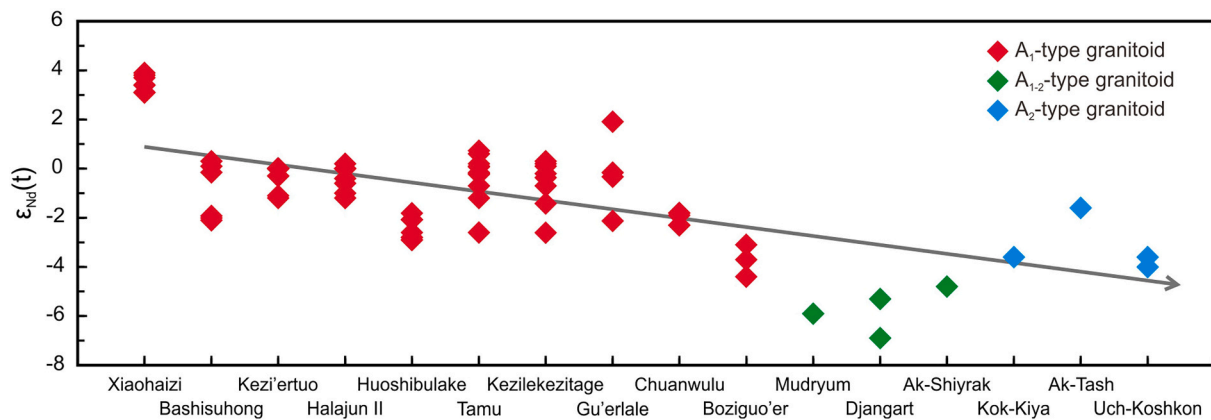
**Fig. 14.** Whole-rock $\varepsilon_{Nd(t)}$ for the A-type granitoids in the Belt and Margin, which exhibits an overall downswing trend from inner TLIP towards STOB. Data of these A-type granitoids are from Huang et al. (2012a, 2012b, 2014), Konopelko et al. (2007), Ma et al. (2016), Wei and Xu (2011), Wei et al. (2019), Zhang et al. (2010), Zhang and Zou (2013) and Zong et al. (2020).

~290 Ma and ~280 Ma. These two magmatic episodes are consistent with the A-type granitoid in the STOB and the margin of Tarim Basin. (2) ~270–300 Ma A-type granitoids have a distribution paralleling with the terminal suture (Fig. 2). The $A_1$-type intrusions are mostly distributed along the terminal suture, which are the thinned and weak zones of the TLIP, e.g., the Bashisuhong, Chuanwulu, Halajun and Xiaohaizi in the east, and Boziguo'er and Keqikeguole in the west (Huang et al., 2012a; Huang et al., 2012b; Huang et al., 2014; Ma et al., 2016; Su et al., 2019; Wei et al., 2019; Yang et al., 2007; Zhang et al., 2010; Zhang and Zou, 2013; Zong et al., 2020). The $A_2$-type granitoids display a far distance away from the terminal suture within the STOB, e.g., Kok-Kiya, Baleigong, At-Tash, Uch-Koshkon, Tashkoro and Baoaozikelike from east to the west (Huo et al., 2019; Konopelko et al., 2007; Konopelko et al., 2009; Long et al., 2008).

The emplaced location of these alkaline intrusions is in the transitional period from a compressive regime to an extensional or post-collisional one in the Late Paleozoic. And these alkaline intrusions coincide with the main active stages of the TLIP. The general consensus of closure time between the South Tienshan plate and the Tarim Block is around the Late Carboniferous (before ~300 Ma) (Gao et al., 2011; Huang et al., 2012a; Konopelko et al., 2009). Thus, the STOB had been in the post-collisional environment when the ultramafic pipes erupted in the Tarim Block at ~300 Ma (Fig. 15a). The plume might also provide dynamics to the extensional motion. At ~290 Ma (Fig. 15b), the orogenic belt was extensional collapse under self-gravity or delamination. As the lithosphere or crustal materials sank into the mantle, the geochemical nature of the mantle was also fertilized. For most A-type granitoids in the STOB, this is agreed with characters of the negative $\varepsilon_{Nd(t)}$ values and the $A_2$-type granitoid. The thinning of the STOB also provided a favorable space for the upwelling convecting mantle of the TLIP in the late or middle stage.

As the Halajun intrusions show the $A_1$-type affinity and low $\delta^{18}O$ values of the Halajun pluton IV quartz-syenite, this indicates that the rising mantle plume plays a more prominent role in generating the Halajun plutons rather than the post-collisional mechanism. At ~280 Ma decompression melting of the mantle plume might take place in thin spots and weak zones (Xu et al., 2014), which might be the terminal suture in the convergent hinge of the South Tienshan plate and the Tarim Block. In the Halajun area (Fig. 15c), the rising mantle magma mixing with a small portion of crust-derived magmas generated the Halajun pluton IV quartz-syenite, and with the incremental volume of crust-derived magmas generated the Kaladuowei plutons.

## 6. Conclusions

(1) The Kaladuowei intrusion consists of two lithofacies, quartz-monzonite and tourmaline-rich granite. Zircon U–Pb dating indicates that the Halajun pluton IV quartz-syenite (283.4 ± 1.1 Ma), Kaladuowei quartz-monzonite (280.2 ± 1.3 Ma) and Kaladuowei tourmaline-rich granite (270.7 ± 1.5 Ma) were formed in the Early Permian.

(2) The geochemical features of quartz-syenite, quartz-monzonite and tourmaline-rich granite display affinities of classical A-type granitoids. The quartz-syenite and quartz-monzonite show representative $A_1$-type affinity. As the crystallization differentiation of ilmenite and biotite in the early-phase, like quartz-monzonite, magmatism of the Kaladuowei intrusion drifts from the $A_1$-type nature to the $A_2$-type in the more evolved tourmaline-rich granite.

(3) The elevated zircon $\delta^{18}O$ values and relative positive $\varepsilon_{Hf(t)}$ values of these A-type granitoids are related to the mixing of mantle-derived magmas and ancient Tarim basement in their parental source. The whole-rock trace element ratios show more middle- to upper-crustal contribution for the final tourmaline-rich granite, and main lower crust for quartz-syenites and quartz-monzonites.

(4) With the high magmatic temperature of these intrusions (790–960 °C) and the lower $\delta^{18}O$ values of quartz-syenite (6.2–6.9‰), the generation of the Halajun $A_1$-type granitoids was more likely related to the contemporaneous Permian Tarim mantle plume.

(5) In the South Tienshan, the Early Permian A-type granitoids have a distribution paralleling with the terminal suture and are associated with the TLIP. The $A_1$-type intrusions are mostly distributed along the terminal suture, where are the thinned and weak zones of the TLIP, e.g., the Bashisuhong, Chuanwulu, Halajun and Xiaohaizi, and Boziguo'er and Keqikeguole. The $A_2$-type granitoids display a far distance away from the terminal suture within the STOB, e.g., Kok-Kiya, Baleigong, At-Tash, Uch-Koshkon, Tashkoro and Baoaozikelike. The whole-rock $\varepsilon_{Nd(t)}$ and zircon $\varepsilon_{Hf(t)}$ values of these granitoids show an overall downswing trend from $A_1$-types to $A_2$-types, and indicate that the involved proportion and the nature of crust compositions could explain the transition from the $A_1$-type granitoid belt to the $A_2$-type granitoid belt. The fractional crystallization of ilmenite and biotite could also enhance the gradual drift from $A_1$-type to $A_2$-type granitoid in different lithofacies.
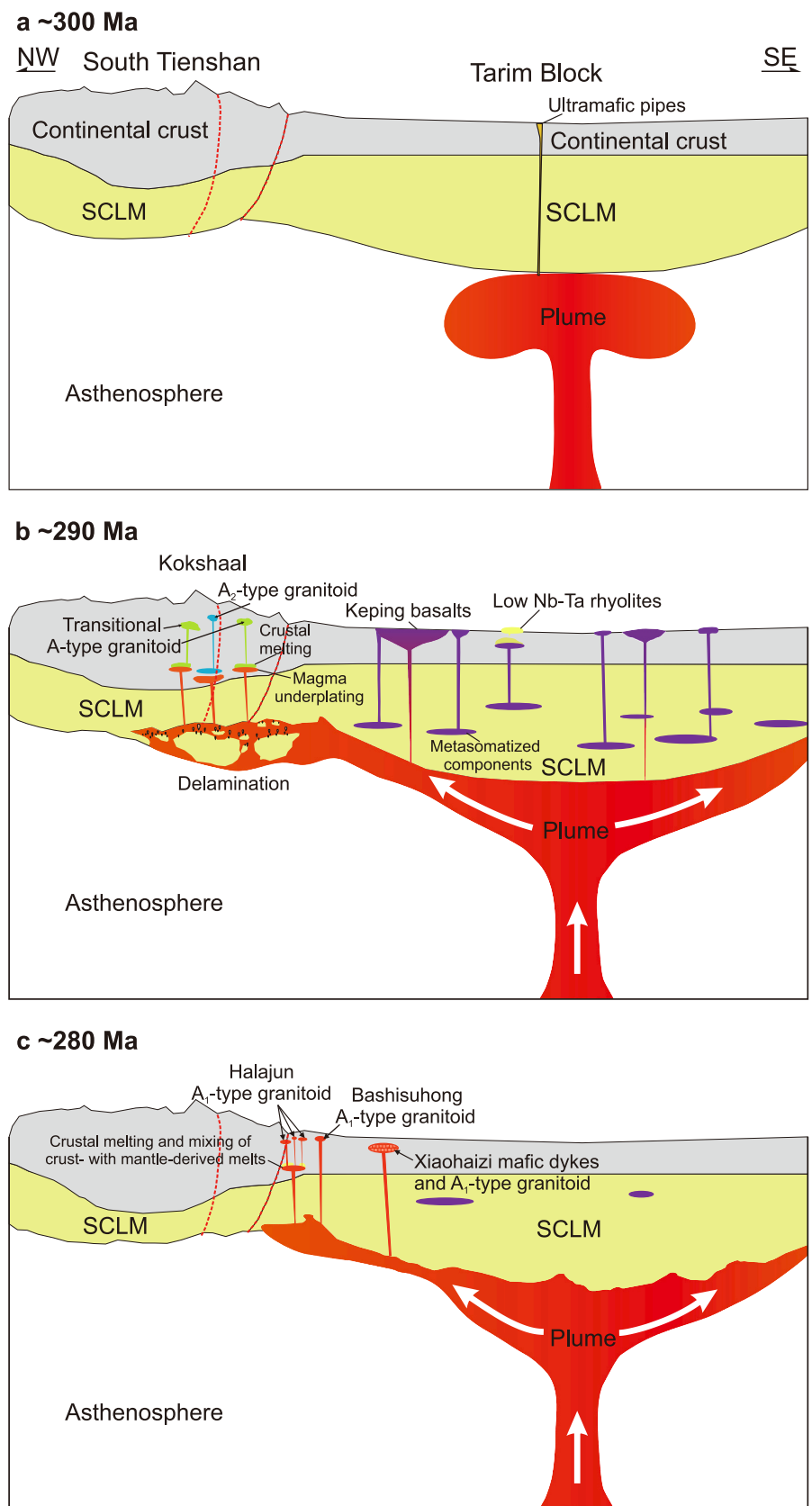
**Fig. 15.** Schematic illustration of the possible petrogenetic model for the different A-type granitoids in the evolution of the STOB and TLIP. (a) At ~300 Ma, the plume rose and the plume head upwelled under the Tarim Block. The plume generated the ultramafic pipes, and also provided dynamic energy to the extensional motion. (b) At ~290 Ma, the collapse of the Tienshan Orogenic Belt and the contemporary heavy eruption of TLIP not only provided channels for the upwelling mantle magma, but also recycled the lithosphere or crustal materials into the mantle, which might involve in the formation of the $A_2$-type and transitional A-type granitoids in the STOB. (c) At ~280 Ma, decompression melting of the mantle plume might take place in the terminal suture in the convergent hinge of the South Tienshan plate and the Tarim Block, which could form the STOB $A_1$-type granitoids. (For interpretation of the references to colour in this figure legend, the reader is referred to the web version of this article.)

## Declaration of Competing Interest

The authors declare that they have no potential conflicts of interest with respect to the research, authorship, and/or publication of this article.

## Acknowledgments

## Appendix A. Supplementary data

Supplementary data to this article can be found online at https://doi.org/10.1016/j.lithos.2023.107333.

## References

Abuduxun, N., Xiao, W.J., Windley, B.F., Chen, Y.C., Huang, P., Sang, M., Li, L., Liu, X.J., 2021. Terminal suturing between the Tarim Craton and the Yili-Central Tianshan Arc: insights from melange-ocean plate stratigraphy, detrital zircon ages, and provenance of the South Tianshan accretionary complex. Tectonics 40.

Acosta-Vigil, A., Buick, I., Hermann, J., Cesare, B., Rubatto, D., London, D., Morgan, G.B., 2010. Mechanisms of crustal anatexis: a geochemical study of partially melted metapelitic enclaves and host dacite, SE Spain. J. Petrol. 51, 785–821.

Allen, M.B., Windley, B.F., Chi, Z., 1992. Palaeozoic collisional tectonics and magmatism of the Chinese Tien Shan, Central Asia. Tectonophysics 220, 89–115.

Ballouard, C., Massuyeau, M., Elburg, M.A., Tappe, S., Viljoen, F., Brandenburg, J.T., 2020. The magmatic and magmatic-hydrothermal evolution of felsic igneous rocks as seen through Nb-Ta geochemical fractionation, with implications for the origins of rare-metal mineralizations. Earth Sci. Rev. 203.

Blichert-Toft, J., 2008. The Hf isotopic composition of zircon reference material 91500. Chem. Geol. 253, 252–257.

Blichert-Toft, J., Albarede, F., 1997. The Lu-Hf isotope geochemistry of chondrites and the evolution of the mantle-crust system. Earth Planet. Sci. Lett. 148, 243–258.

Boehnke, P., Watson, E.B., Trail, D., Harrison, T.M., Schmitt, A.K., 2013. Zircon saturation re-revisited. Chem. Geol. 351, 324–334.

Bonin, B., 2007. A-type granites and related rocks: evolution of a concept, problems and prospects. Lithos 97, 1–29.

Chappell, B.W., 1996. Compositional variation within granite suites of the Lachlan fold belt: its causes and implications for the physical state of granite magma. Trans. R. Soc. Edinb. Earth Sci. 87, 159–170.

Charvet, J., Shu, L.S., Laurent-Charvet, S., Wang, B., Faure, M., Cluzel, D., Chen, Y., Jong, K.D., 2011. Palaeozoic tectonic evolution of the Tianshan belt, NW China. Sci. China Earth Sci. 54, 166–184.

Collins, W.J., Beams, S.D., White, A.J.R., Chappell, B.W., 1982. Nature and origin of A-type granites with particular reference to southeastern Australia. Contrib. Mineral. Petrol. 80, 189–200.

Collins, W.J., Huang, H.Q., Bowden, P., Kemp, A.I.S., 2019. Repeated S- I- A-type granite trilogy in the Lachlan Orogen, and geochemical contrasts with A-type granites in Nigeria: implications for petrogenesis and tectonic discrimination. Geol. Soc. Lond. Spec. Publ. 491. SP491-2018-2159.

Dobretsov, N.L., 2003. Mantle plumes and their role in the formation of anorogenic granitoids. Geol. Geofiz. 44, 1243–1261.

Eby, G.N., 1990. The A-type granitoids: a review of their occurrence and chemical characteristics and speculations on their pedogenesis. Lithos 26, 115–134.

Eby, G.N., 1992. Chemical subdivision of the A-type granitoids: petrogenetic and tectonic implications. Geology 20, 641–644.

Fedele, L., Lustrino, M., Melluso, L., Morra, V., Zanetti, A., Vannucci, R., 2015. Trace-element partitioning between plagioclase, alkali feldspar, Ti-magnetite, biotite, apatite, and evolved potassic liquids from Campi Flegrei (Southern Italy). Am. Mineral. 100, 233–249.

Frindt, S., Haapala, I., Pakkanen, L., 2004. Anorogenic Gross Spitzkoppe granite stock in central western Namibia: part I. Petrology and geochemistry. Am. Mineral. 89, 841–856.

Frost, B.R., Barnes, C.G., Collins, W.J., Arculus, R.J., Ellis, D.J., Frost, C.D., 2001. A geochemical classification for granitic rocks. J. Petrol. 42, 2033–2048.

Gao, J., Li, M.S., Xiao, X.C., Tang, Y.Q., He, G.Q., 1998. Paleozoic tectonic evolution of the Tianshan Orogen, northwestern China. Tectonophysics 287, 213–231.

Gao, J., Klemd, R., Qian, Q., Zhang, X., Li, J.L., Jiang, T., Yang, Y.Q., 2011. The collision between the Yili and Tarim blocks of the Southwestern Altaids: geochemical and age constraints of a leucogranite dike crosscutting the HP-LT metamorphic belt in the Chinese Tianshan Orogen. Tectonophysics 499, 118–131.

Ge, R.F., Zhu, W.B., Wilde, S.A., He, J.W., Cui, X., 2015. Synchronous crustal growth and reworking recorded in late Paleoproterozoic granitoids in the northern Tarim craton:

in situ zircon U-Pb-Hf-O isotopic and geochemical constraints and tectonic implications. Geol. Soc. Am. Bull. 127, 781–803.

Griffin, W.L., Pearson, N.J., Belousova, E., Jackson, S.E., van Achterbergh, E., O'Reilly, S. Y., Shee, S.R., 2000. The Hf isotope composition of cratonic mantle: LAM-MC-ICPMS analysis of zircon megacrysts in kimberlites. Geochim. Cosmochim. Acta 64, 133–147.

Han, B.F., He, G.Q., Wang, X.C., Guo, Z.J., 2011. Late Carboniferous collision between the Tarim and Kazakhstan-Yili terranes in the western segment of the South Tian Shan Orogen, Central Asia, and implications for the Northern Xinjiang, western China. Earth Sci. Rev. 109, 74–93.

Hole, M.J., 2018. Mineralogical and geochemical evidence for polybaric fractional crystallization of continental flood basalts and implications for identification of peridotite and pyroxenite source lithologies. Earth Sci. Rev. 176, 51–67.

Hu, Z.C., Liu, Y.S., Gao, S., Liu, W.G., Zhang, W., Tong, X.R., Lin, L., Zong, K.Q., Li, M., Chen, H.H., Zhou, L., Yang, L., 2012. Improved in situ Hf isotope ratio analysis of zircon using newly designed X skimmer cone and jet sample cone in combination with the addition of nitrogen by laser ablation multiple collector ICP-MS. J. Anal. At. Spectrom. 27, 1391–1399.

Huang, H., Zhang, Z., Kusky, T., Santosh, M., Zhang, S., Zhang, D., Liu, J., Zhao, Z., 2012a. Continental vertical growth in the transitional zone between South Tianshan and Tarim, western Xinjiang, NW China: insight from the Permian Halajun A1-type granitic magmatism. Lithos 155, 49–66.

Huang, H., Zhang, Z.C., Kusky, T., Zhang, D.Y., Hou, T., Liu, J.L., Zhao, Z.D., 2012b. Geochronology and geochemistry of the Chuanwulu complex in the South Tianshan, western Xinjiang, NW China: implications for petrogenesis and phanerozoic continental growth. Lithos 140, 66–85.

Huang, H., Zhang, Z., Santosh, M., Zhang, D., 2014. Geochronology, geochemistry and metallogenic implications of the Boziguo'er rare metal-bearing peralkaline granitic intrusion in South Tianshan, NW China. Ore Geol. Rev. 61, 157–174.

Huo, H.L., Chen, Z.L., Zhang, Q., Han, F.B., Zhang, W.G., Sun, Y., Yang, B., Tang, Y.W., 2019. Chronological constraints on late Paleozoic collision in the Southwestern Tianshan Orogenic Belt, China: evidence from the Baleigong granites. Acta Geol. Sin. Engl. Ed. 93, 1188–1204.

Jiang, T., Gao, J., Klemd, R., Qian, Q., Zhang, X., Xiong, X.M., Wang, X.S., Tan, Z., Chen, B.X., 2014. Paleozoic ophiolitic melanges from the South Tianshan Orogen, NW China: geological, geochemical and geochronological implications for the geodynamic setting. Tectonophysics 612, 106–127.

Jiang, X.Y., Wu, K., Luo, J.C., Zhang, L.P., Sun, W.D., Xia, X.P., 2020. An A(1)-type granite that borders A(2)-type: insights from the geochemical characteristics of the Zongyang A-type granite in the lower Yangtze River Belt, China. Int. Geol. Rev. 62, 2203–2220.

Klemd, R., Gao, J., Li, J.L., Meyer, M., 2015. Metamorphic evolution of (ultra)-high-pressure subduction-related transient crust in the South Tianshan Orogen (Central Asian Orogenic Belt): geodynamic implications. Gondwana Res. 28, 1–25.

Konopelko, D., Biske, G., Seltmann, R., Eklund, O., Belyatsky, B., 2007. Hercynian post-collisional A-type granites of the Kokshaal Range, Southern Tien Shan, Kyrgyzstan. Lithos 97, 140–160.

Konopelko, D., Seltmann, R., Biske, G., Lepekhina, E., Sergeev, S., 2009. Possible source dichotomy of contemporaneous post-collisional barren I-type versus tin-bearing A-type granites, lying on opposite sides of the South Tien Shan suture. Ore Geol. Rev. 35, 206–216.

Lebas, M.J., Lemaitre, R.W., Streckeisen, A., Zanettin, B., 1986. A chemical classification of volcanic rocks based on the total alkali–silica diagram. J. Petrol. 27, 745–750.

Li, X.H., Liu, Y., Li, Q.L., Guo, C.H., Chamberlain, K.R., 2009. Precise determination of Phanerozoic zircon Pb/Pb age by multicollector SIMS without external standardization. Geochem. Geophys. Geosyst. 10.

Li, X.H., Long, W.G., Li, Q.L., Liu, Y., Zheng, Y.F., Yang, Y.H., Chamberlain, K.R., Wan, D. F., Guo, C.H., Wang, X.C., Tao, H., 2010. Penglai zircon megacrysts: a potential new working reference material for microbeam determination of Hf-O isotopes and U-Pb age. Geostand. Geoanal. Res. 34, 117–134.

Li, Z.L., Chen, H.L., Song, B.A., Li, Y.Q., Yang, S.F., Yu, X., 2011. Temporal evolution of the Permian large igneous province in Tarim Basin in northwestern China. J. Asian Earth Sci. 42, 917–927.

Liu, Y.S., Hu, Z.C., Gao, S., Gunther, D., Xu, J., Gao, C.G., Chen, H.H., 2008. In situ analysis of major and trace elements of anhydrous minerals by LA-ICP-MS without applying an internal standard. Chem. Geol. 257, 34–43.

Liu, Y.S., Gao, S., Hu, Z.C., Gao, C.G., Zong, K.Q., Wang, D.B., 2010. Continental and oceanic crust recycling-induced melt-peridotite interactions in the trans-North China Orogen: U-Pb dating, Hf isotopes and trace elements in zircons from mantle xenoliths. J. Petrol. 51, 537–571.

Liu, H.Q., Xu, Y.G., He, B., 2013. Implications from zircon-saturation temperatures and lithological assemblages for early Permian thermal anomaly in Northwest China. Lithos 182, 125–133.

Liu, H.Q., Xu, Y.G., Tian, W., Zhong, Y.T., Mundil, R., Li, X.H., Yang, Y.H., Luo, Z.Y., Shang-Guan, S.M., 2014. Origin of two types of rhyolites in the Tarim Large Igneous Province: consequences of incubation and melting of a mantle plume. Lithos 204, 59–72.

Liu, H.Q., Xu, Y.G., Zhong, Y.T., Luo, Z.Y., Mundil, R., Riley, T.R., Zhang, L., Xie, W., 2019. Crustal melting above a mantle plume: insights from the Permian Tarim Large Igneous Province, NW China. Lithos 326, 370–383.

Loiselle, M.C., Wones, D.R., 1979. Characteristics and origin of anorogenic granites. Geol. Soc. Am. Abstr. Programs 11, 468.

Long, L.L., Gao, J., Wang, J.B., Qing, Q., Xiong, X.M., Wang, Y.W., Wang, L.J., Gao, L.M., 2008. Geochemistry and SHRIMP zircon U-Pb age of post-collisional granites in the Southwest Tianshan orogenic belt of China: examples from the Heiyingshan and Laohutai plutons. Acta Geol. Sin. Engl. Ed. 82, 415–424.

Long, L.L., Gao, J., Klemd, R., Beier, C., Qian, Q., Zhang, X., Wang, J., Jiang, T., 2011. Geochemical and geochronological studies of granitoid rocks from the Western Tianshan Orogen: implications for continental growth in the southwestern Central Asian Orogenic Belt. Lithos 126, 321–340.

Ma, L.T., Zhang, Z.C., Dong, S.Y., Zhang, S., Zhang, D.Y., Huang, H., Xue, C.J., 2009. Yingmailai granitic intrusion in the Southern Tianshan: magnetite-series or ilmentie-series? Geoscience 23, 1039–1048.

Ma, Y., Zhang, Z.C., Huang, H., Santosh, M., Cheng, Z.G., 2016. Petrogenesis of the Bashisuogong bimodal igneous complex in southwest Tianshan Mountains, China: implications for the Tarim Large Igneous Province. Lithos 264, 509–523.

Maniar, P.D., Piccoli, P.M., 1989. Tectonic discrimination of granitoids. Geol. Soc. Am. Bull. 101, 635–643.

Markl, G., Marks, M.A.W., Frost, B.R., 2010. On the controls of oxygen fugacity in the generation and crystallization of peralkaline melts. J. Petrol. 51, 1831–1847.

Middlemost, E.A.K., 1994. Naming materials in the magma/igneous rock system. Earth Sci. Rev. 37, 215–224.

Morel, M.L.A., Nebel, O., Nebel-Jacobsen, Y.J., Miller, J.S., Vroon, P.Z., 2008. Hafnium isotope characterization of the GJ-1 zircon reference material by solution and laser-ablation MC-ICPMS. Chem. Geol. 255, 231–235.

Nash, W.P., Crecraft, H.R., 1985. Partition coefficients for trace elements in silicic magmas. Geochim. Cosmochim. Acta 49, 2309–2322.

Satybaev, M., Ding, L., Takasu, A., Bakirov, A., Sakiev, K., Cai, F., Orozbaev, R., Bakirov, A., Baslakunov, J., 2018. Petrology of metamorphic rocks from the Atbashy complex, Southern Tien-Shan, Kyrgyzstan. Geosci. Front. 9, 1795–1807.

Seltmann, R., Konopelko, D., Biske, G., Divaev, F., Sergeev, S., 2011. Hercynian post-collisional magmatism in the context of Paleozoic magmatic evolution of the Tien Shan orogenic belt. J. Asian Earth Sci. 42, 821–838.

Solomovich, L.I., Trifonov, B.A., 2002. Postcollisional granites in the South Tien Shan Variscan Collisional Belt, Kyrgyzstan. J. Asian Earth Sci. 21, 7–21.

Stepanov, A.S., Hermann, J., 2013. Fractionation of Nb and Ta by biotite and phengite: implications for the "missing Nb paradox". Geology 41, 303–306.

Su, Y.P., Zheng, J.P., Liang, L., Dai, H., Zhao, J., Chen, M., Ping, X., Liu, Z., Wang, J., 2019. Derivation of A1-type granites by partial melting of newly underplated rocks related with the Tarim mantle plume. Geol. Mag. 156, 409–429.

Sun, S.S., McDonough, W.F., 1989. Chemical and isotopic systematics of oceanic basalts: implications for mantle composition and processes. Geol. Soc. Lond. Spec. Publ. 42.

Tagiri, M., Yano, T., Bakirov, A., Nakajima, T., Uchiumi, S., 1995. Mineral Parageneses and Metamorphic P-T Paths of Ultrahigh-Pressure Eclogites from Kyrghyzstan Tien-Shan, 4, pp. 280–292.

Valley, J.W., Kinny, P.D., Schulze, D.J., Spicuzza, M.J., 1998. Zircon megacrysts from kimberlite: oxygen isotope variability among mantle melts. Contrib. Mineral. Petrol. 133, 1–11.

Wang, B., Jahn, B.M., Lo, C.H., Shu, L.S., Wu, C.Y., Li, K.S., Wang, F., 2011a. Structural analysis and Ar-40/Ar-39 thermochronology of Proterozoic rocks in Sailimu area (NW China): implication to polyphase tectonics of the North Chinese Tianshan. J. Asian Earth Sci. 42, 839–853.

Wang, B., Shu, L., Faure, M., Jahn, B.-M., Cluzel, D., Charvet, J., Chung, S.-L., Meffre, S., 2011b. Paleozoic tectonics of the southern Chinese Tianshan: insights from structural, chronological and geochemical studies of the Heiyingshan ophiolitic melange (NW China). Tectonophysics 497, 85–104.

Wei, X., Xu, Y.G., 2011. Petrogenesis of Xiaohaizi syenite complex from Bachu area, Tarim. Acta Petrol. Sin. 27, 2984–3004.

Wei, X., Xu, Y.G., Feng, Y.X., Zhao, J.X., 2014. Plume-lithosphere interaction in the generation of the Tarim Large Igneous Province, NW China: geochronological and geochemical constraints. Am. J. Sci. 314, 314–356.

Wei, X., Xu, Y.G., He, B., Zhang, L., Xia, X.P., Shi, X.F., 2019. Zircon U-Pb age and Hf-O isotope insights into genesis of Permian Tarim felsic rocks, NW China: implications for crustal melting in response to a mantle plume. Gondwana Res. 76, 290–302.

Whalen, J.B., Currie, K.L., Chappell, B.W., 1987. A-type granites: geochemical characteristics, discrimination and petrogenesis. Contrib. Mineral. Petrol. 95, 407–419.

Windley, B.F., Allen, M.B., Zhang, C., Zhao, Z.Y., Wang, G.R., 1990. Paleozoic accretion and Cenozoic redeformation of the Chinese Tien Shan Range, Central Asia. Geology 18, 128–131.

Xiao, W.J., Windley, B.F., Sun, S., Li, J.L., Huang, B.C., Han, C.M., Yuan, C., Sun, M., Chen, H.L., 2015. A tale of amalgamation of three permo-triassic collage systems in Central Asia: oroclines, sutures, and terminal accretion. In: Jeanloz, R., Freeman, K. H. (Eds.), Annual Review of Earth and Planetary Sciences, vol. 43, pp. 477–507.

Xiong, X.L., Keppler, H., Audetat, A., Ni, H.W., Sun, W.D., Li, Y.A., 2011. Partitioning of Nb and Ta between rutile and felsic melt and the fractionation of Nb/Ta during partial melting of hydrous metabasalt. Geochim. Cosmochim. Acta 75, 1673–1692.

Xiong, S.Q., Yang, H., Ding, Y.Y., Li, Z.K., Li, W., 2016. Distribution of igneous rocks in China revealed by aeromagnetic data. J. Asian Earth Sci. 129, 231–242.

Xu, Y.G., Wei, X., Luo, Z.Y., Liu, H.Q., Cao, J., 2014. The early Permian Tarim Large Igneous Province: main characteristics and a plume incubation model. Lithos 204, 20–35.

Yang, S.F., Li, Z.L., Chen, H.L., Santosh, M., Dong, C.W., Yu, X., 2007. Permian bimodal dyke of Tarim Basin, NW China: geochemical characteristics and tectonic implications. Gondwana Res. 12, 113–120.

Yu, X., Yang, S.F., Chen, H.L., Chen, Z.Q., Li, Z.L., Batt, G.E., Li, Y.Q., 2011. Permian flood basalts from the Tarim Basin, Northwest China: SHRIMP zircon U-Pb dating and geochemical characteristics. Gondwana Res. 20, 485–497.

Zhang, C.L., Zou, H.B., 2013. Permian A-type granites in Tarim and western part of Central Asian Orogenic Belt (CAOB): genetically related to a common Permian mantle plume? Lithos 172, 47–60.

Zhang, L.F., Ai, Y.L., Li, X.P., Rubatto, D., Song, B., Williams, S., Song, S.G., Ellis, D., Liou, J.G., 2007. Triassic collision of western Tianshan orogenic belt, China: evidence from SHRIMP U-Pb dating of zircon from HP/UHP eclogitic rocks. Lithos 96, 266–280.

Zhang, C.L., Xu, Y.G., Li, Z.X., Wang, H.Y., Ye, H.M., 2010. Diverse Permian magmatism in the Tarim Block, NW China: genetically linked to the Permian Tarim mantle plume? Lithos 119, 537–552.

Zhang, D.Y., Zhang, Z.C., Mao, J.W., Huang, H., Cheng, Z.G., 2016. Zircon U-Pb ages and Hf-O isotopic signatures of the Wajilitag and Puchang Fe-Ti oxide-bearing intrusive complexes: constraints on their source characteristics and temporal-spatial evolution of the Tarim Large Igneous Province. Gondwana Res. 37, 71–85.

Zonenshain, L.P., Kuzmin, M.I., Natapov, L.M., 1990. Geology of the USSR: A Plate-Tectonic Synthesis, 21. American Geophysics Union, Washington, DC, pp. 1–242.

Zong, Z.J., Du, Y.S., Li, S.T., Cao, Y., Du, J.G., Deng, X.H., Xue, L.W., 2020. Petrogenesis of the early Permian A-type granites in the Halajun region, southwest Tianshan, western Xinjiang, NW China: implications for geodynamics of Tarim Large Igneous Province. Int. Geol. Rev. 63, 1–22.